https://doi.org/10.5194/egusphere-2025-4330
Preprint. Discussion started: 27 November 2025

On the Mechanisms that Control the Rainy Season Transition Periods in the Equatorial Congo Basin

Sarah Worden[1,2], Rong Fu[2]

[1]Jet Propulsion Laboratory, California Institute of Technology, Pasadena, 91109, USA
[2]Atmospheric and Oceanic Sciences Department, University of California Los Angeles, Los Angeles, 90095, USA

Correspondence to: Sarah Worden (sarah.r.worden@jpl.nasa.gov)

Abstract. The Congo Basin equatorial region (2°S-2°N, within the watershed), experiences semi-annual rainy seasons (RSs) in boreal spring and fall. Previously, the mechanisms driving the transitions to these RSs have not been investigated systematically. We show that both RS transitions begin with increases in the low-level atmospheric moisture transport from the Atlantic Ocean into the region, ~1.5 months prior to the spring RS and ~2 months prior to the fall RS. Evapotranspiration contributes the most to atmospheric moisture but does not change significantly throughout both transition periods. Sharp precipitation jumps 10 days before the start of the spring and fall RSs result from boundary layer moisture increases orographically uplifted to the lower troposphere by the East African Rift and Congo Basin Cell ascending branch. This destabilizes the lower free troposphere, lowering the level of free convection and decreasing convective inhibitive energy. Meanwhile, the African Easterly Jet-North and westerly return flow of the Congo Basin Cell induce vertical shear for the spring and fall RSs, respectively. Mid-tropospheric convergence strengthens due to return flow at ~700 hPa from shallow meridional cells that direct low-level moisture towards the West African Heat Low prior to the spring RS, and to the Congo Air Boundary prior to the fall RS. Therefore, the RS onsets over the equatorial region are driven by seasonal changes in large-scale atmospheric circulation, contrasting with the pivotal role of increasing evapotranspiration in driving the transition to the RS onset over the southern Congo Basin.

1 Introduction

The Congo Basin is a global water and carbon centre hosting vast rainforest, rivers, and precipitation (Brummett et al., 2009; Alsdorf et al., 2016; Xu et al., 2021). However, due to a lack of in situ data and limited infrastructure for research (Alsdorf et al., 2016), its meteorology and hydrological cycle have been less studied compared to the rest of Africa (Washington et al., 2013; Biasutti, 2019; Biasutti and Sobel, 2009; Lv et al., 2024; Seth et al., 2013; Yang et al., 2015; Thorncroft et al., 2011). Most studies examining process controls on seasonal rainfall have focused on the rainy seasons (Nicholson, 2022; Cook and Vizy, 2022; Pokam Mba et al., 2022). As such, the processes that control the transition to the rainy season onsets are virtually unknown. To fundamentally understand observed rainfall variability (Jiang et al., 2019; Zhou et al., 2014; Hua et al., 2016; 2018) within the equatorial region (defined as the area between 2°S-2°N, within the

https://doi.org/10.5194/egusphere-2025-4330
Preprint. Discussion started: 27 November 2025

Congo Basin watershed), which experiences two rainy seasons, in boreal spring and fall, respectively (Fig. 1; Pokam Mba et al., 2022; Nicholson, 2022), necessitates a full understanding of the mechanisms controlling its seasonal rainfall.

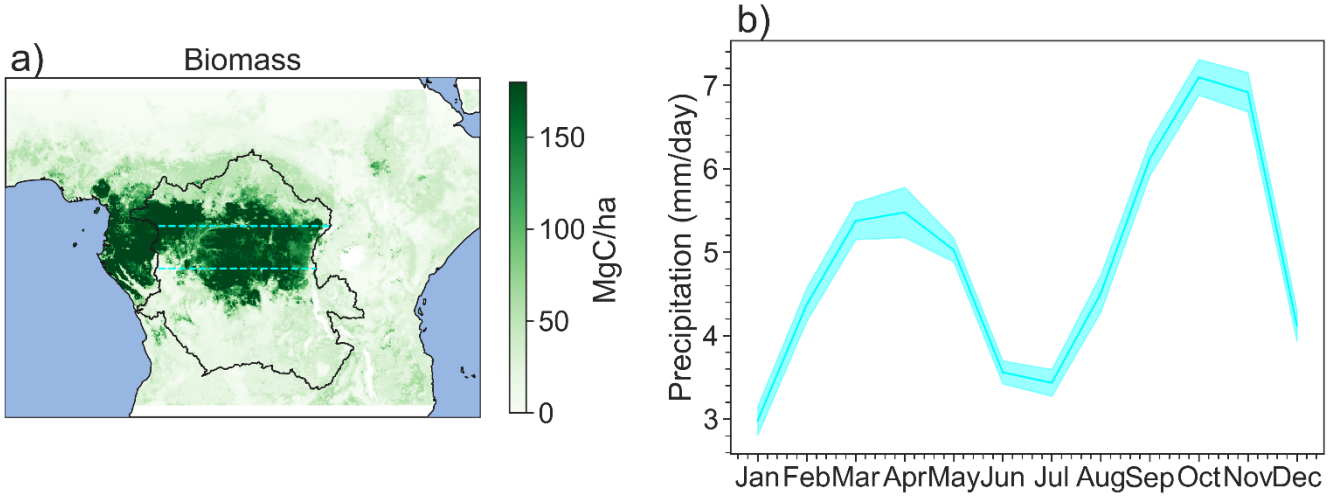

Figure 1: (a) Above-ground biomass averaged between 2000-2019. Black outline denotes the Congo Basin watershed and the dashed lines at $2°S$ and $2°N$ represent the boundary of the equatorial region. (b) Precipitation climatology for the equatorial region. Shades are the standard error of the mean over of the different years.

The equatorial Congo Basin is unique in that its rainy seasons are not associated with strong surface moisture flux convergence (Nicholson, 2018; Yang et al., 2015). Instead, near-surface moisture diverges away from the equatorial Congo basin, while mid-tropospheric moisture convergence appears to be central for rainfall formation (Nicholson, 2022). Atmospheric moisture for rainfall mainly comes from evapotranspiration (ET) both within Congo basin and from the adjacent land (e.g., Risi et al., 2016; Sorí et al., 2022; van der Ent et al., 2010; Worden et al., 2021), though moisture transport from the surrounding oceans is important for its rainy seasons as well (e.g., Pokam et al., 2012). Several dynamic systems play important roles: a shallow zonal circulation referred to as the Congo Basin Cell (Longandjo and Rouault, 2020), the Congo Air Boundary (Howard and Washington, 2019) where warm, humid air from the Congo meets with relatively cool and dry air from the subtropical southern hemispheric Africa, the African Easterly Jet North and South (AEJ-N, AEJ-S; Nicholson, 2022; Chen 2005; Kuete et al., 2020), a deep Walker-like zonal circulation (Longandjo and Rouault, 2020), and shallow meridional overturning cells (Longandjo and Rouault, 2023). Additionally, the East African Rift helps to induce uplift of near surface air and hence precipitation on the Congo Basin's eastern boundary (Nicholson, 2022).

However, the moisture contributions from land and terrestrial sources, and the presence and intensity of these dynamical systems vary throughout the year, likely leading to differences in the mechanisms controlling the transitions to the spring and fall rainy seasons. For example, the annual presence of the zonal Congo Basin Cell is debated. While Longandjo and Rouault (2020) argue that the cell is present year-round, Neupane (2016) and Cook and Vizy (2016) indicate that it is present only in the second half of the year. The Congo Air Boundary is strongest between August-October, and weakest between December-January (Howard and Washington, 2019). The AEJ-N is present year-round but moves latitudinally such

https://doi.org/10.5194/egusphere-2025-4330
Preprint. Discussion started: 27 November 2025

that it is centred near the equator during the spring rainy season but centred outside of the Congo Basin around 10°N during the fall rainy season (Kuete et al., 2020; Nicholson and Grist, 2003). The AEJ-S only develops in the boreal fall in September (Kuete et al., 2020).

The influences of the heat lows over Sahara and Kalahari Desert, respectively, on the equatorial Congo region also change between the two rainy seasons, which is important for meridional moisture transport. During the fall rainy season, the southern African dry heat low is centred over the plateau region as the Angola heat low, but prior to the spring rainy season, a moist Angola thermal low migrates to the Kalahari region to become the Kalahari heat low (Howard and Washington, 2018; 2019; Attwood et al., 2024). Meanwhile, the northern hemisphere West African heat low is centred around the Sahelian region during the spring rainy season (around $10°N - 15°N$). During the fall rainy season, it transitions back towards the northern Congo Basin (Lavaysse et al., 2009). The different position of the heat lows can affect meridional moisture flow in and out of the basin (Cook et al., 2020). The mechanisms controlling the transition periods to the rainy seasons likely reflect the seasonal presence or movement of these key features.

ET provides about 70% of the atmospheric moisture over the Congo basin (e.g., van de Ent et al. 2010; Risi et al. 2013; Worden et al. 2021), and as much as 83% of the atmospheric moisture in February and March, during the transition to spring rainy season. Worden and Fu (2025) further shows that, over the Southern Congo ($2°S - 14°S, 15°E - 30°E$), the increase of ET driven by increasing surface solar radiation plays a pivotal role to increase moisture in the atmospheric boundary layer, which, in turn, increases deep convection and leads to rainy season onset in boreal fall. On the other hand, most previous studies emphasize increasing moisture transport as a potential key driver for the rainy season (e.g., Pokam et al. 2012; Nicholson and Dezfuli, 2013; Balas et al., 2007). For the equatorial Congo basin, whether ET plays a similar role as over the Southern Congo basin has been unclear. In this study, we will investigate the roles of the aforementioned dynamic and thermodynamic processes in driving the transition to the spring and fall wet seasons, respectively, over the equatorial Congo basin.

2 Data and Methods

2.1 Data

We use satellite data and reanalysis products in our study. We resample all the daily data to 5-day pentads, except for the Tropospheric Emission Spectrometer (TES) data, in which we use daily HDO and H2O measurements in this analysis instead of pentad measurements as the number of observations is limited compared to the other products. For all other datasets, we average our products over 2000-2018 or 2003-2018 depending on when the datasets are available.

The TES data requires quality control processing described here: the following quality flags were used when retrieving the data from the TES satellite: “Species Retrieval Quality = 1,” “Degrees of Freedom for Signal >1,” and “Average Cloud Optical Depth <0.4” to ensure good quality data as suggested by Worden et al. (2012). The accuracy of these data is ~6 per mil with a precision of 20 per mil (Worden et al., 2012) for the vertical range used in this analysis (~900-

https://doi.org/10.5194/egusphere-2025-4330
Preprint. Discussion started: 27 November 2025

420 hPa, or about 1-6 km above sea level). We use data between 2005-2011 when the quality of estimates is suitable for our analysis (Worden et al., 2021).

Source	Data	Resolution	Years	Reference
Tropical Rainfall Measuring Mission (TRMM) 3B42/3B43	Precipitation	0.25° × 0.25° Daily, Monthly	2000-2020	Huffman et al., 2007
Atmospheric Infrared Sounder (AIRS) L3 V7 Standard Physical Retrieval Ascending TqJoint	atmospheric-layer mass mixing ratio, surface mass mixing ratio, atmospheric-layer relative humidity, atmospheric-layer temperature	1° × 1° Daily	2003-2018	Aumann et al., 2019, Pagano et al., 2003, Irion et al., 2018, DeSouza-Machado et al., 2018
Clouds and the Earth's Radiant Energy System (CERES) Syn1deg Ed 4.1	cloud top temperature, cloud top height, cloud area fraction (total, high, mid-high, mid-low, and low)	1° × 1° Daily	2003-2018	Doelling, et al., 2013, Doelling et al., 2016, Su, et al., 2005, Rutan et al., 2015
Global Land Evaporation Amsterdam Model (GLEAM) v3.7b	Evapotranspiration	0.25 × 0.25° daily	2000-2018	Martens et al., 2017, Miralles et al., 2011
Ground plots, lidar, global modeling, and satellite data	Aboveground biomass	0.1 × 0.1° yearly	2000-2018	Xu et al., 2021
Tropospheric Emission Spectrometer version 6 (v006_Litev01.00)	Deuterium (HDO), water vapor (H_2O)	Level 2 daily	2005-2011	Worden et al., 2012, Worden et al., 2021
European Centre for Medium-Range Weather Forecasts (ECMWF) ERA5	zonal and meridional (u and v) winds, vertically integrated moisture flux convergence, total column water vapor (CWV), vertical velocity, divergence, temperature, vertical integral of eastward total water vapour flux, vertical integral of northward total water vapour flux, and specific humidity	0.25° × 0.25° daily	2000-2018	Hersbach et al., 2020

Table 1: Data used in this study.

https://doi.org/10.5194/egusphere-2025-4330
Preprint. Discussion started: 27 November 2025

2.2 Methods

2.2.1 Calculating the Onsets and Ends of the Rainy Seasons

Using TRMM precipitation data, we calculate the rainy season onsets and ends (RSOs and RSEs, respectively) in the equatorial Congo Basin similar to the approach used in Chakraborty et al. (2021), originally developed by Li and Fu (2004), for RSOs and RSEs in the Amazon. This definition is designed to capture persistently high rainfall during the rainy season and persistent low rainfall in the dry season using the annual mean rainfall as the threshold. We first calculate the climatological pentad (5 day mean) rainfall for each year over our domain, then determine the rainy season onsets and ends in the following steps.

For the spring rainy season, the onset is defined as the first pentad of each year that meets the following criterion: four out of the previous six pentads are less than the climatological annual mean, and four out of the following seven pentads are more than the climatological annual mean. Likewise, the end of the spring rainy season is defined as the first pentad of each year that meets the following criterion: four out of the previous six pentads are more than the climatological annual mean, and four out of the following seven pentads are less than the climatological annual mean.

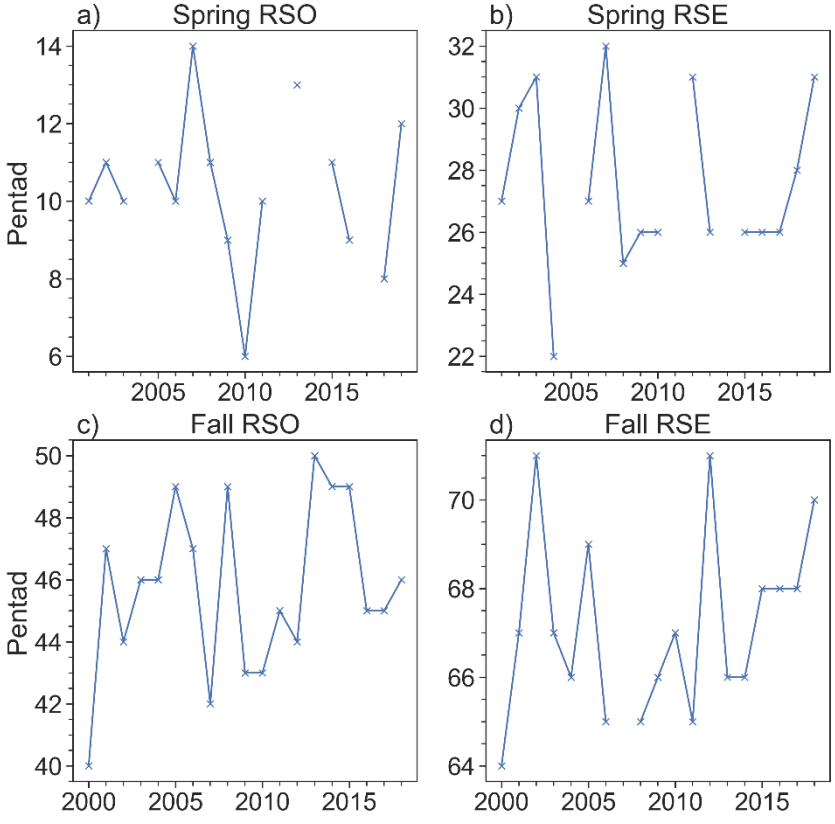

Figure 2: Pentad starts of the RSOs and RSEs for the equatorial Congo: (a) Spring RSOs; (b) Spring RSEs; (c) Fall RSOs; d) Fall RSEs.

https://doi.org/10.5194/egusphere-2025-4330
Preprint. Discussion started: 27 November 2025

For the fall rainy season, the onset is defined as the first pentad of each year that meets the following criterion: six out of the previous eight pentads are less than the climatological annual mean, and six out of the following eight pentads are more than the climatological annual mean. The fall RSE is defined as the first pentad of each year that meets the following criterion: six out of the previous eight pentads are more than the climatological annual mean, and six out of the following eight pentads are less than the climatological annual mean. We note that this criterion for the fall rainy seasons differs from that of the spring rainy season because the latter is shorter and weaker than that of the fall rainy season (Fig. 2). Therefore, a shorter period and less persistent threshold was needed to best capture the starts and ends of persistently high and low rainfall for the spring RSO and RSE.

Figure 2 shows the RSOs and RSEs for the spring and fall rainy seasons between the years 2000-2020. We excluded the year 2000 when calculating the spring RSO because we needed to consider the ends of the prior years in our RSO calculations. Similarly, we excluded the year 2020 when calculating the fall RSE because we needed to consider the start of the next years in our RSE calculations. We additionally excluded from our following analyses any years during which a RSO or RSE was unable to be identified, or if the length of a rainy season was less than 5 pentads. The spring RSO ranges from the 6th to 14th pentad (with Days 1-5 defined as Pentad "0"), corresponding to early-February to mid-March. On average, the spring RSO occurs on 25 February-2 March. The spring RSE ranges from the 22nd-32nd pentads, corresponding to late-April to mid-June. On average, the spring RSE occurs on 21 May-25 May. The fall RSO ranges from the 40th-50th pentads, corresponding to mid-July to early-September. On average, the fall RSO occurs on 29 August-2 September. The fall RSE ranges from the 64th-71st pentads, corresponding to mid-November to late-December. On average, the fall RSE occurs on 2 December-6 December. There are no overlaps between the fall RSO and the spring RSE, as well as between the spring RSO and the fall RSE. There are 19 pentads between the average spring RSO and fall RSE and 20 pentads between the average fall RSO and spring RSE. We show 15 pentads prior to the spring RSO and 19 pentads prior to the fall RSO as these periods capture the key changes in processes that drive the dry to rainy season transition as in Li and Fu (2004) and Wright et al. (2017).

2.2.2 Computation of Key Variables

We calculate the area-mean equivalent potential temperature (θ_e) from AIRS gridded data at daily time resolution to examine atmospheric instability during and after the transition to the rainy season. We calculate θ_e using the following equation from Bolton (1980):

$$\theta_e = T_k \left(\frac{1000}{p}\right)^{0.2854\left(1-0.28\times10^{-3}*r\right)} \times exp\left[\left(\frac{3.376}{T_L} - 0.00254\right) \times r(1 + 0.81 \times 10^{-3} r)\right] \quad \text{Eq. 1}$$

Where T_k is the absolute temperature (K) at pressure level p, p is pressure (hPa), r is the mixing ratio (g/kg), T_L is the absolute temperature at the lifting condensation level (K) calculated by the following:

$$T_L = \frac{2840}{3.5 ln T_{k0} - lne - 4.805} + 55 \quad \text{Eq. 2}$$

https://doi.org/10.5194/egusphere-2025-4330
Preprint. Discussion started: 27 November 2025

Where $e = \frac{p*r}{622+r}$ is the water vapor pressure, and here T_{k0} is the absolute temperature at the surface, defined here as 925 hPa as the surface of the equatorial region is above sea level. We use the AIRS mass mixing ratio, temperature, and pressure in these calculations. We similarly calculate saturated equivalent potential temperature θ_{e_s} by letting $r = r_s$, where r_s is the saturated mixing ratio. We calculate r_s by the following:

We calculate e_s as in Bolton (1980):

$$e_s = 6.112exp\left(\frac{17.67T}{T+243.5}\right) \quad \text{Eq. 3}$$

Where T is the temperature in Celsius ($°C$). We calculate saturated vapor pressure by:

$$r_s = \frac{\varepsilon e_s}{p-e_s} \quad \text{Eq. 4}$$

Where $\varepsilon = 0.622$ is ratio of molar masses of vapor and dry air, and e_s is the saturation vapor pressure, calculated as in Bolton (1980):

$$e_s(T) = 6.112\exp\left(\frac{17.67T}{T+243.5}\right) \quad \text{Eq. 5}$$

We also calculate moist static energy (MSE) where MSE is represented by:

$$MSE = c_pT + Lq + gz. \quad \text{Eq. 6}$$

Where c_p is the specific heat capacity at constant pressure, L is the latent heat of evaporation and g is gravity. Finally, we examine changes in moisture in the equatorial Congo with the following:

We examine vertically integrated moisture flux (MF) transport, $MF = \int_{p_s}^{p_{TOA}} q \cdot \vec{V} dp$, where q is the specific humidity and $\vec{V}$**=(u,v),** is the horizontal wind, with u the zonal, and v the meridional wind component, respectively. P_s denotes the surface pressure and P_{TOA} denotes the pressure of the top of the atmosphere. We examine the net zonal $MF = \int_{p_s}^{p_{TOA}} q \cdot udp$ across the western and eastern boundaries of the equatorial Congo basin. We also examine the net meridional $MF = \int_{p_s}^{p_{TOA}} q \cdot vdp$ across its northern and southern boundaries. For simplicity, we choose the northern boundary along $2°N$ and between $14 - 30°E$, and the southern boundary along $2°S$ and between $14 - 30°E$. The western boundary is along $14°$ E and between $2°S - 2°N$ and the eastern boundary is along $30°$ E and between $2°S - 2°N$. To be able to compare to vertically integrated MF convergence, we calculate the length between the western/eastern boundaries and the northern/southern boundaries, respectively. However, the distance between the zonal boundaries is about four times larger than the distance between the meridional boundaries. Therefore, we divide the zonal difference by four as a best approximation of the divergence calculation for MF. Finally, we calculate the first component of the moisture convergence term ($-q \times \nabla.\vec{V}$) and moisture transport vectors ($q\vec{V}$) averaged between different pressure levels to represent the lower and middle tropospheric moisture transport.

2.2.3 Examining the ET Contribution to Atmospheric Moisture

Due to a lack of reliable ET measurements, we use the deuterium content of water (HDO) derived from satellite measurements and an isotope mixing model to estimate the fractional contribution of ET to atmospheric moisture. HDO is

https://doi.org/10.5194/egusphere-2025-4330
Preprint. Discussion started: 27 November 2025

expressed as the relative ratio of the number of HDO molecules to the total number of H_2O molecules in parts per thousand (‰) relative to the isotopic composition of ocean water as shown below:

$$\delta D = 1000 \times \left(\frac{R - R_{std}}{R_{std}}\right) \quad \text{Eq. 7}$$

Where R is of the ratio of HDO molecules to the total number of H_2O molecules and R_{std} is the corresponding ratio in a reference standard, taken here to be the Vienna Standard Mean Ocean Water: $R_{std} = 3.11 \times 10^{-4}$ (e.g. Wright et al., 2017 and references therein). The isotopic composition of water vapor in the free troposphere is due to a mixture of air parcels originating from different sources (Galewsky, 2018; Galewsky and Hurley, 2010). We can use the isotopic composition of an air mass to trace its source to either vegetation or ocean because δD values from ocean evaporation are distinctively different from those by rainforest ET. Atmospheric moisture coming from transpiration will generally be more isotopically enriched (or heavier) than evaporation because lighter isotopes preferentially evaporate (Risi et al., 2020; Tremoy et al., 2014; Worden et al., 2007). However, observed values of free-tropospheric deuterium content also depend on atmospheric processes, such as the type of convection present, described further in Galewsky et al. (2016). This is because they vary by the first order with changes in specific humidity (Bailey et al., 2017).

Therefore, we compare the observed isotopic composition of water vapor in the free troposphere to two models, a mixing model and a Rayleigh model, to identify which air parcels are likely influenced by land (i.e., transpiration) versus ocean (i.e., evaporated water; Noone, 2012). A mixing model describes what happens to a mixture of two air masses with different water vapor isotopic compositions. Meanwhile, under the Rayleigh distillation model, as an air mass moves upward (or towards cooler conditions), condensate enriched with heavy isotope is completely removed immediately after it forms under the assumption of pseudo adiabatic process (Galewsky et al., 2016; Wright et al., 2017). A further description of these models can be found in the Supplementary and in S. Worden et al. (2021).

3 Results

3.1 Transition from the Dry Season to the Spring RSO

3.1.1 Early Transition

The first part of the spring transition, i.e., the early-transition period, starts with a turning point from strengthening to weakening vertically integrated MF divergence (Fig. 3a) 10 pentads (50 days) before the spring RSO. To explain this weakening, we evaluate net zonal and meridional MF (Fig. 3c). Negative values indicate net moisture leaving the basin for both net zonal MF and net meridional MF. Variations in net zonal MF during the early transition period are driven by increases in low-level moisture transport from the Atlantic Ocean, by the lower branch of the Congo Basin Cell, which goes through the equatorial Congo, towards the West African Heat Low (Lavaysse et al., 2009) in the northern Congo (Fig. 4a, b; Fig. B1a, e). This is driven by increasing near-surface temperature gradients between the Atlantic Ocean and West African Heat Low (Fig. S1a, b; Fig. S2). These increases in low-level moisture transport, combined with increases in the second half

https://doi.org/10.5194/egusphere-2025-4330
Preprint. Discussion started: 27 November 2025

of the transition period of mid-level moisture transport into the basin across its eastern boundary, acts against zonal moisture leaving the basin at mid-levels, across the western boundary (Fig. B1a, b), but is not enough to lead to net zonal MF convergence (Fig. 3c). Meridionally, mid-level moisture entering the basin across the northern boundary does not change
200 significantly, although low-level moisture leaving the basin across the northern boundary increases in response to increased low-level moisture transport towards the West African Heat Low (Fig. 4a, b; Fig. B1c, f). Across the southern boundary, moisture transport entering the basin at low levels increases, while moisture transport leaving the basin at mid-levels does not significantly change (Fig. B1d, f). Ultimately, it is changes in low-level meridional moisture transport that drive changes in net meridional MF divergence (Fig. 3c).

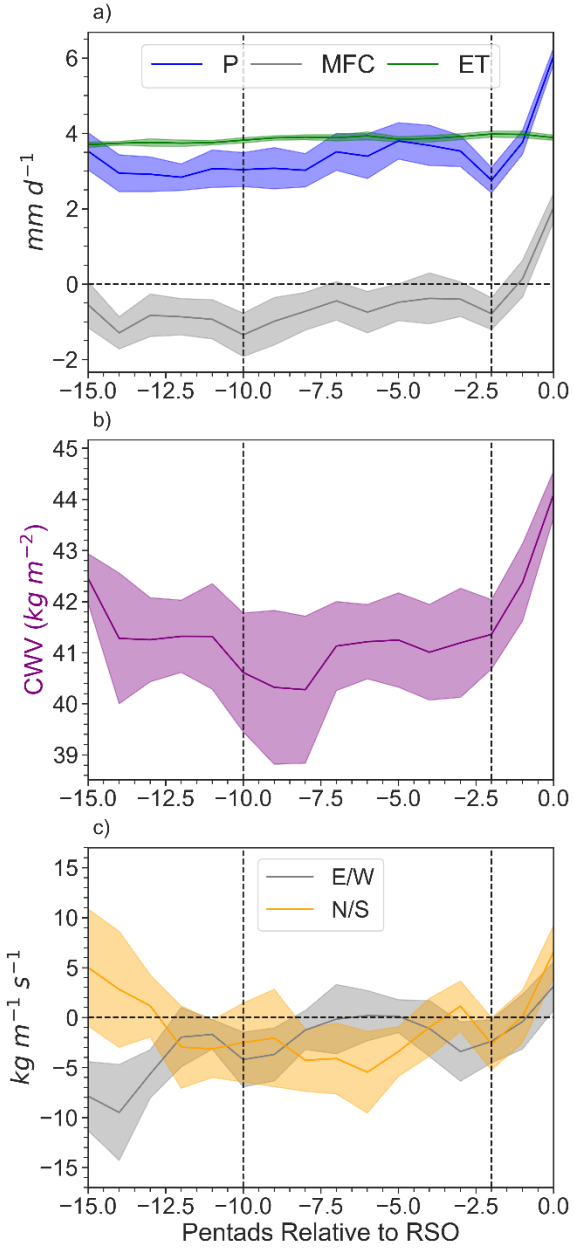

https://doi.org/10.5194/egusphere-2025-4330
Preprint. Discussion started: 27 November 2025

Figure 3: For the transition to the spring RSO: (a) Precipitation (P), vertically integrated MF convergence, and evapotranspiration (ET); (b) column water vapor (CWV); and (c) Net MF across the zonal and meridional boundaries (E/W: East minus West; N/S: North minus South; Methods). Positive means convergence, negative means divergence. All are relative to the RSO (denoted as '0' in the graph). Time series are smoothed using a Savitsky-Golay filter (number of coefficients: 5, polynomial order 2). Shades represents the standard error of the mean of the different years.

Meanwhile, ET does not change significantly compared to the pre-transition ($f_{mix_{pre}} = 0.761 \pm 0.082$; $f_{mix_{early}} = 0.764 \pm 0.112$), but is clearly the dominant contributor to moisture (Fig. 5a, b). This is consistent with S. Worden et al., (2021) for a similar domain. Therefore, ET is important for maintaining high background moisture while weakening in MF divergence initiates the transition to the spring rainy season onset.

Furthermore, the atmosphere appears thermodynamically primed for deep convection, with large convective available potential energy and conditional instability as shown by $\frac{d\theta_e}{dp} < 0$ (Fig. 6c, d). However, weak ascent or even subsidence still exists above 650 hPa (Fig. 6e). Additionally, the level of free convection (LFC; Fig. 7a), and therefore convective inhibitive energy (Fig. 6c) do not change significantly throughout the early transition period. This indicates that the atmospheric conditions, especially the dynamic conditions, are still not ready for large-scale increases of deep convection and subsequently, rainfall.

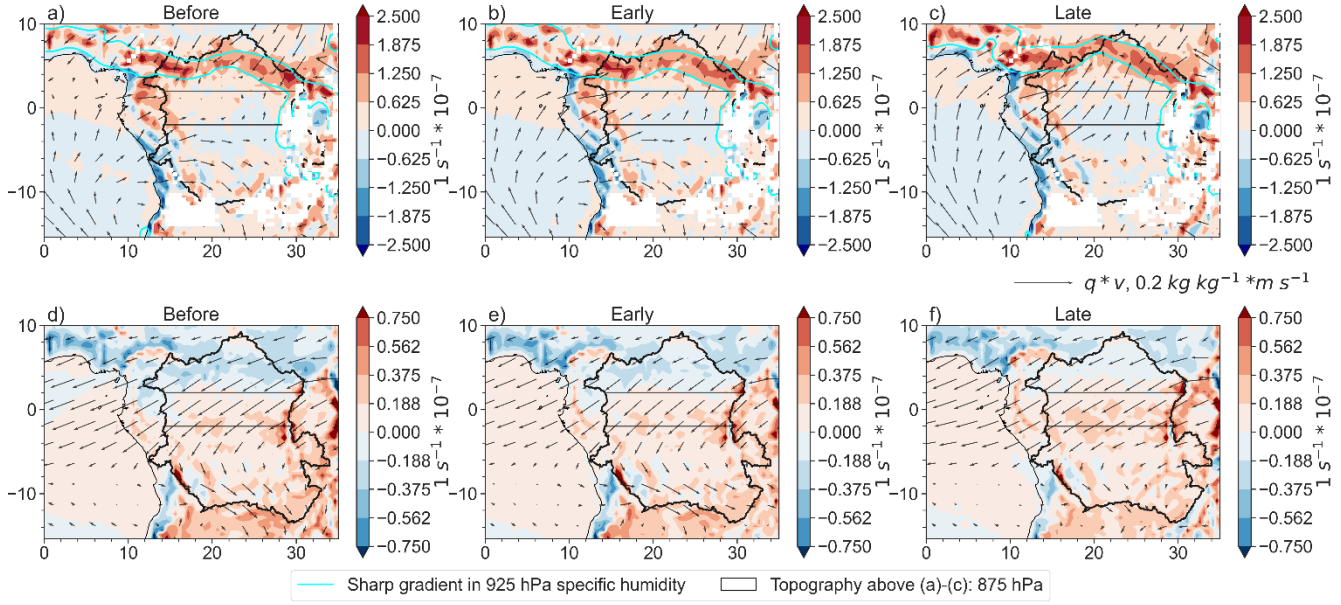

Figure 4: Moisture transport vectors ($q * v$) and moisture convergence ($q * DIV$; shades, positive means convergence) for (a)-(c) average of 925-875 hPa for the "before," early, and late transition period, respectively; (d)-(f) average of 850-600 hPa for the "before," early, and late transition period, respectively. Vectors are scaled up by a factor of 2 to better visualize the changes in magnitude and direction between periods. White masks in (a)-(c) represent areas where the elevation is higher than 875 hPa. Aqua contours in (a)-(c) represent sharp 925 hPa specific humidity gradients, which overlap with the area of convergence.

https://doi.org/10.5194/egusphere-2025-4330
Preprint. Discussion started: 27 November 2025

We explain this as following: with weakening atmospheric MF divergence, boundary layer specific humidity begins to increase (Fig. 7d), due to increases in moisture transport from the equatorial Atlantic Ocean into the equatorial Congo (Fig. 4a, b). The increase of boundary layer moisture, rather than increase of near-surface temperature, drives boundary layer
230 increases in MSE (Fig. 7b-d). However, at the mid-levels, MSE initially decreases and then increases in mid-level specific humidity (Fig. 7b), which is driven by mid-level moisture divergence. Therefore, while the boundary layer MSE is favourable for deep convection, additional changes are needed to support deep convection in the mid-layers of the atmosphere.

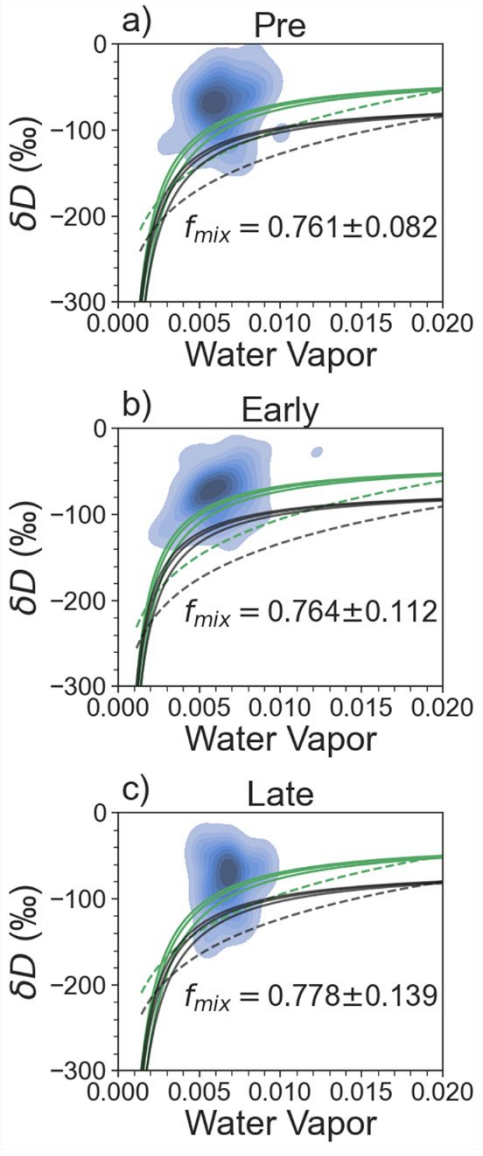

https://doi.org/10.5194/egusphere-2025-4330
Preprint. Discussion started: 27 November 2025

Figure 5: Fraction of observed δD above a series of mixing (solid) and Rayleigh (dashed) models. Green indicates land-based water vapor models, while black indicates ocean-based water vapor models. f_{mix} is the fraction of observed δDabove the uppermost, land-based mixing model. For (a) the "before" period (15-11 pentads prior to the spring RSO); (b) the early-transition; and (c) the late-transition.

3.1.2 Late Transition Period

The late-transition period starts with a rapid increase in atmospheric column water vapor (CWV; Fig. 3b), a key condition for deep convection (Bretherton et al., 2004; Schiro et al., 2018). This is accompanied by rapid increases in P and vertically integrated MF convergence (Fig. 3a). ET does not change significantly ($f_{mix_{late}} = 0.778 \pm 0.139$; Fig. 5c), revealing the importance of large-scale circulation changes in altering atmospheric moisture over the equatorial Congo prior to the spring rainy season.

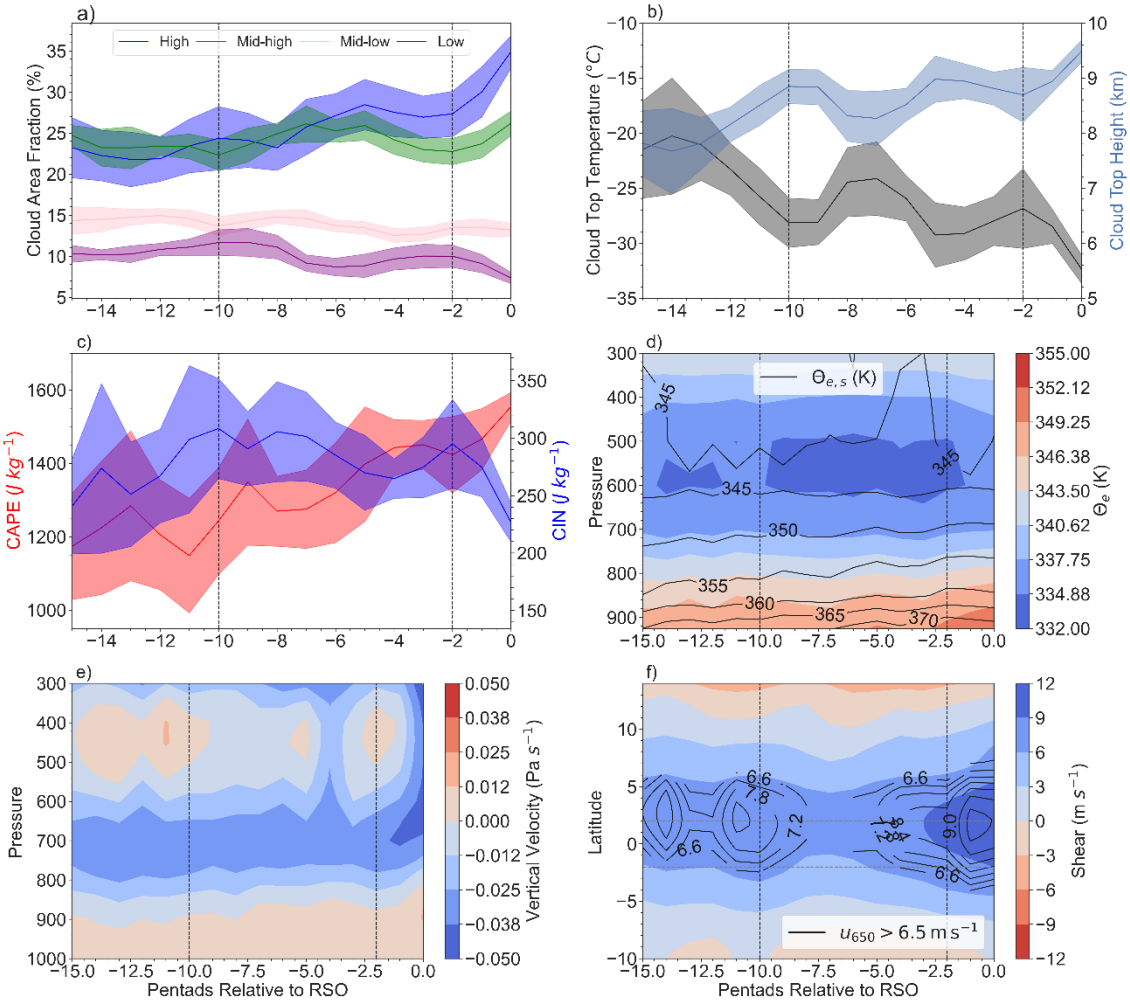

Figure 6: Prior to the spring RSO: (a) cloud area fraction for high, mid-high, mid-low, and low clouds; (b) cloud top temperature and cloud top height; (c) convective available potential energy; and convective inhibitive energy; (d) equivalent potential temperature (θ_e; shades) and saturated equivalent potential temperature (θ_{e_s}); e) vertical

https://doi.org/10.5194/egusphere-2025-4330
Preprint. Discussion started: 27 November 2025

velocity; and f) black contours: 650 hPa zonal wind (u_{650}) greater than $6.5\ m\ s^{-1}$, denoting the AEJ-N. Shaded contours represent the wind shear ($u_{900} - u_{650}$). Shades of the time series in a)-c) represent the standard error of the mean of the different years. All the time series have been smoothed using a Savitsky-Golay filter (number of coefficients: 5, polynomial order 2).

Net meridional and zonal MF rapidly switch from divergence towards convergence (Fig. 3c). Zonally, further increases in near surface temperatures over the West African Heat Low drive stronger LLWs from the Atlantic and across the equatorial region along the way (Fig. B1a; Fig. S1c; Fig. S2; Fig. 4c). This, together with increases in mid-level (above 800 hPa) zonal moisture transport across the eastern boundary (Fig. B1b) compensate the increases in mid-level moisture transport leaving the basin across the western boundary (Fig. B1a). The latter is likely due to the formation of the AEJ-N (Fig. 6f). Therefore, zonal MF becomes convergent, although weakly so (Fig. 3c). Meridionally, moisture transport entering the basin at low levels through the southern boundary increases (Fig. B1c), bringing with it moist air from the southern Congo (Fig. S3c), which is experiencing its rainy season during this time (Worden and Fu, 2025). However, moisture transport leaving the basin across its northern boundary towards the West African Heat Low increases as well (Fig. B1d), leading to net low level meridional moisture transport out of the basin (Fig. 4c). In contrast, moisture convergence at mid-levels increases (Fig. 4f) as mid-level moisture leaving the basin across the southern boundary decreases (Fig. B1d, f). All together, this leads to net meridional MF convergence (Fig. 3c).

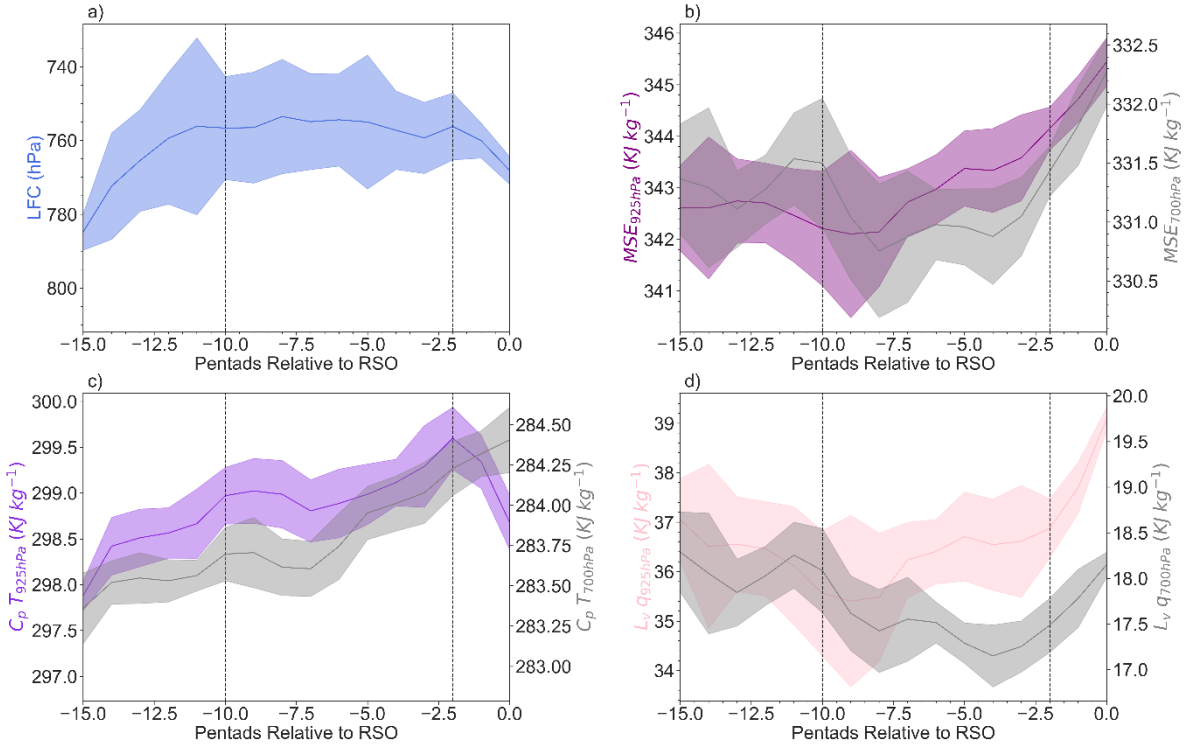

Figure 7: Evolution of (a) the level of free convection (LFC); (b) MSE at 925 hPa and 700 hPa; (c) MSE component C_pT 925 hPa and 700 hPa; and (d) MSE component L_vq at 925 hPa and 700 hPa. All are relative to the spring RSO,

https://doi.org/10.5194/egusphere-2025-4330
Preprint. Discussion started: 27 November 2025

averaged between $14°E - 26°E$ to avoid topography errors in the calculations, and smoothed using the Savitsky-Golay filter. Shades represent the standard error of the mean of the different years.

These changes in atmospheric moisture transport increase boundary layer moisture, as indicated by increasing relative humidity (Fig. 8a, b), but subsidence from the surface to ~850 hPa (Fig. 6e; Fig. 8a, b) between $10°E - 26°E$ (west of the East African Rift) likely prevents this moisture from being uplifted within large parts of the interior equatorial region. Instead increases in westerly wind within the interior of the region pushes this moisture towards the East African Rift (Fig. 8), where orographic lifting forces this moist air into the free troposphere above 800 hPa. Additionally, moisture is uplifted by the ascending branch of the Congo Basin Cell over the equatorial coastline (highlands of Gabon and Cameroon) at the western edge of the equatorial Congo (Fig. 8). Therefore, this results in increasing mid-level moisture and mid-level MSE while decreasing LFC and convective inhibitive energy (Fig. 6c; Fig. 7a, b, d). Upward vertical velocity increases in strength starting in the mid-levels and reaches 300 hPa for the first time (Fig. 6e). Meanwhile, shear increases with the increasing strength of the AEJ-N (Fig. 6f), thus creating conditions favourable for deep convection and the start of the spring rainy season. This is indicated by increases in high clouds, increases in cloud top height, and decreases in cloud top temperature (Fig. 6a, b).

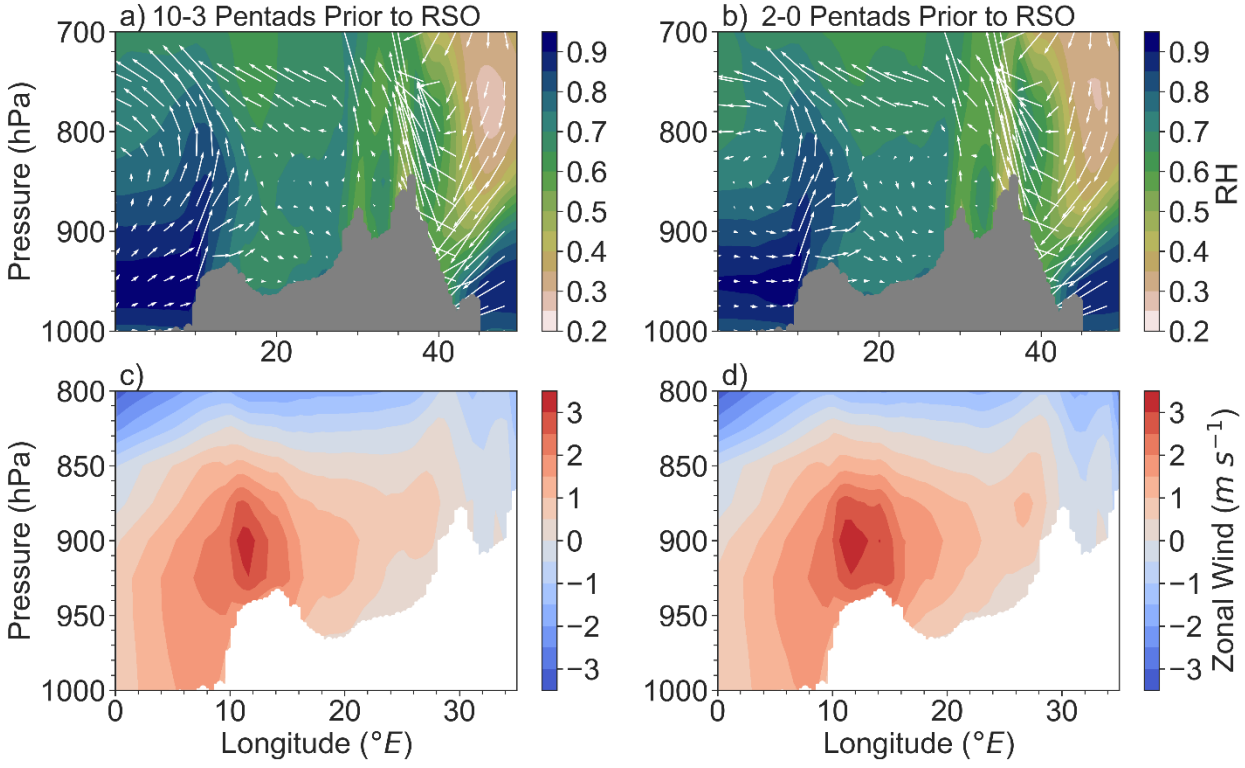

Figure 8: Relative humidity (shades) and vectors of u and $\omega * 10^2$ for (a) 10-3 pentads prior to the spring RSO; (b) 2-0 pentads prior to the spring RSO. Zonal wind (u) for (c) 10-3 pentads prior to the spring RSO; (d) 2-0 pentads prior to the spring RSO. Grey shading in (a)-(b) and white shading in (c)-(d) denotes the topography of the region.

https://doi.org/10.5194/egusphere-2025-4330
Preprint. Discussion started: 27 November 2025

3.2 Transition from the Dry Season to the Fall RSO

3.2.1 Early Transition Period

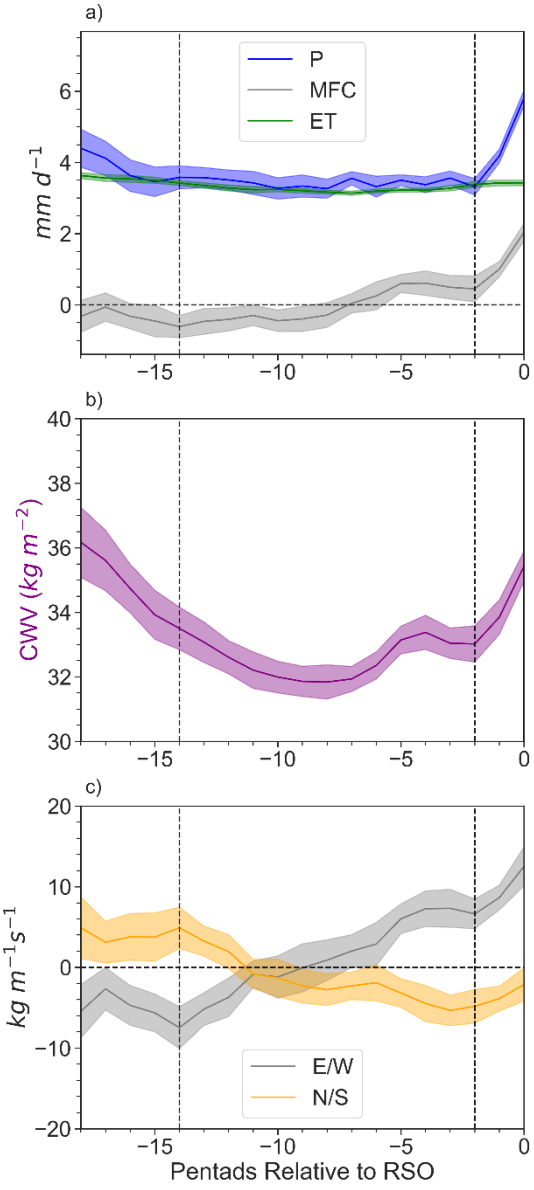

Figure 9: For the transition to the fall RSO: (a) Precipitation (P), vertically integrated MF convergence, and evapotranspiration (ET); (b) column water vapor (CWV); (c) Net MF across the zonal (East minus West) and meridional (North minus South) boundaries (Methods). Positive means convergence, negative means divergence. All

https://doi.org/10.5194/egusphere-2025-4330
Preprint. Discussion started: 27 November 2025

are relative to the RSO (denoted as '0' in the graph). All have been smoothed using a Savitsky-Golay filter (number of coefficients: 5, polynomial order 2). Shades represents the standard error of the mean of the different years.

As in the transition to the spring RSO, the early-transition period starts 14 pentads before the fall RSO with weakening in vertically integrated MF divergence over the equatorial Congo (Fig. 9a), indicated reduced moisture export out of the region. This is mainly due to decreases in net zonal MF divergence (Fig. 9c), which becomes convergent about halfway through the early transition period. This acts against the change of net meridional MF, which starts convergent and switches to divergence during the transition period (Fig. 9c).

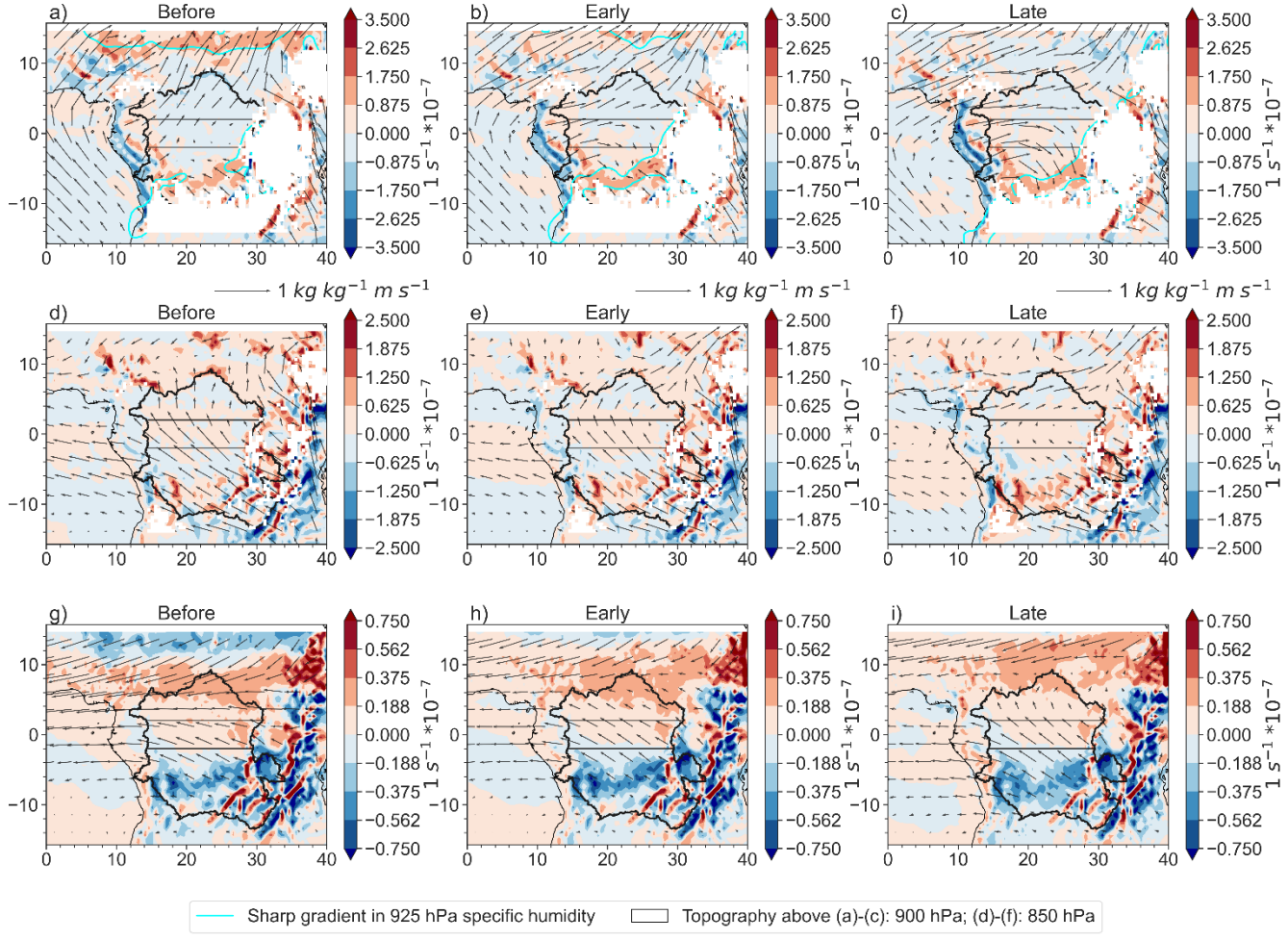

Figure 10: (a)-(c) average of 925-875 hPa. The westerly winds represent the lower branch inflow of the Congo Basin Cell; the aqua shades denote areas of sharp 925 hPa specific humidity gradients. The southern aqua gradients therefore note the rough location of the Congo Air Boundary. (d)-f) average of 850-800 hPa; and (g)-i) average of 775-600 hPa. The easterly winds represent the upper branch return flow of the Congo Basin Cell. Winds have been multiplied by a scale factor of 2 in all panels. Area of convergence between 4°S and 8°S in a-c) represents the rough location of the Congo Air Boundary (CAB). Mainly zonal moisture transport between 6°N – 15°N represents the AEJ-N

https://doi.org/10.5194/egusphere-2025-4330
Preprint. Discussion started: 27 November 2025

Changes in initial net zonal MF divergence are primarily due to increases in low-level moisture transport into the basin, across the western boundary (Fig. 10a, b; Fig. B2a), which combined with steady moisture transport between 800-600 hPa into the basin across the eastern boundary (Fig. B2b), acts against weakly decreasing moisture transport out of the western boundary above 800 hPa (Fig. B2a) via the return branch of the Congo Basin Cell (Longandjo et al., 2020). Increases in low-level atmospheric moisture across the western boundary are driven by the near-surface temperature gradient between the Atlantic Ocean and the equatorial and southern Congo (Fig. S4a, b; Fig. S5), which strengthens the lower branch of the Congo Basin Cell (Longandjo and Rouault, 2020).

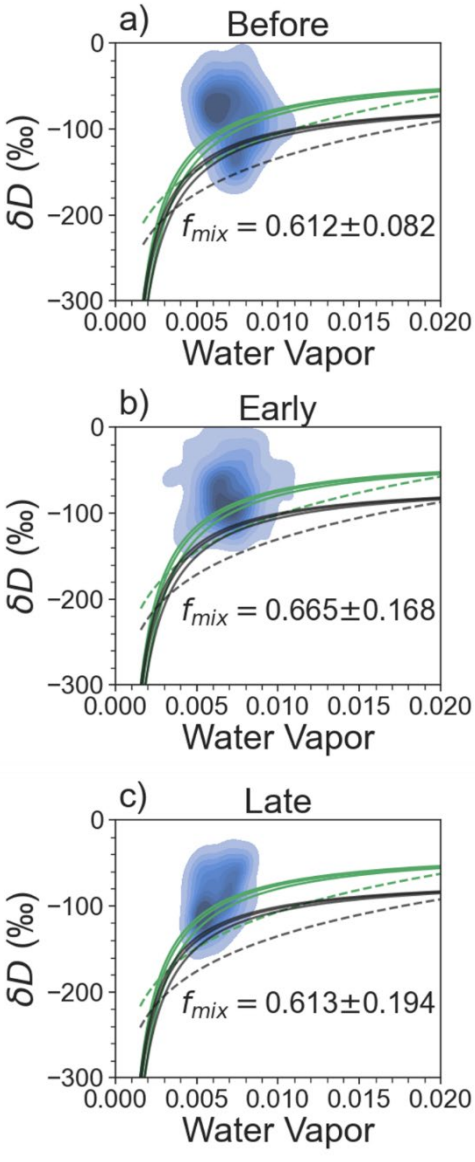

Figure 11: Fraction of observed δD above a series of mixing (solid) and Rayleigh (dashed) models. Green indicates land-based water vapor models, while black indicates ocean-based water vapor models. f_{mix} is the fraction of

https://doi.org/10.5194/egusphere-2025-4330
Preprint. Discussion started: 27 November 2025

observed δD above the uppermost, land-based mixing model. For (a) the "before" period (15-11 pentads prior to the fall RSO); (b) the early-transition; and (c) the late-transition.

Net meridional MF divergence weakens towards zero (Fig. 9c). Across the southern boundary, moisture transport leaving the basin at low levels increases (Fig. B2d, f), moving towards the Congo Air Boundary (aqua contours in Fig. 10b denote sharp surface humidity gradients that show the rough location of the Congo Air Boundary; Howard and Washington, 2019) and associated low-level convergence band (Fig. 10b). Additionally, moisture transport into the equatorial Congo across the southern boundary, above 850 hPa, decreases in strength (Fig. 10d, e). This acts against increases in low-level moisture entering the basin across the northern boundary (Fig. B2d). Together, this causes the net meridional MF divergence by the end of the transition period.

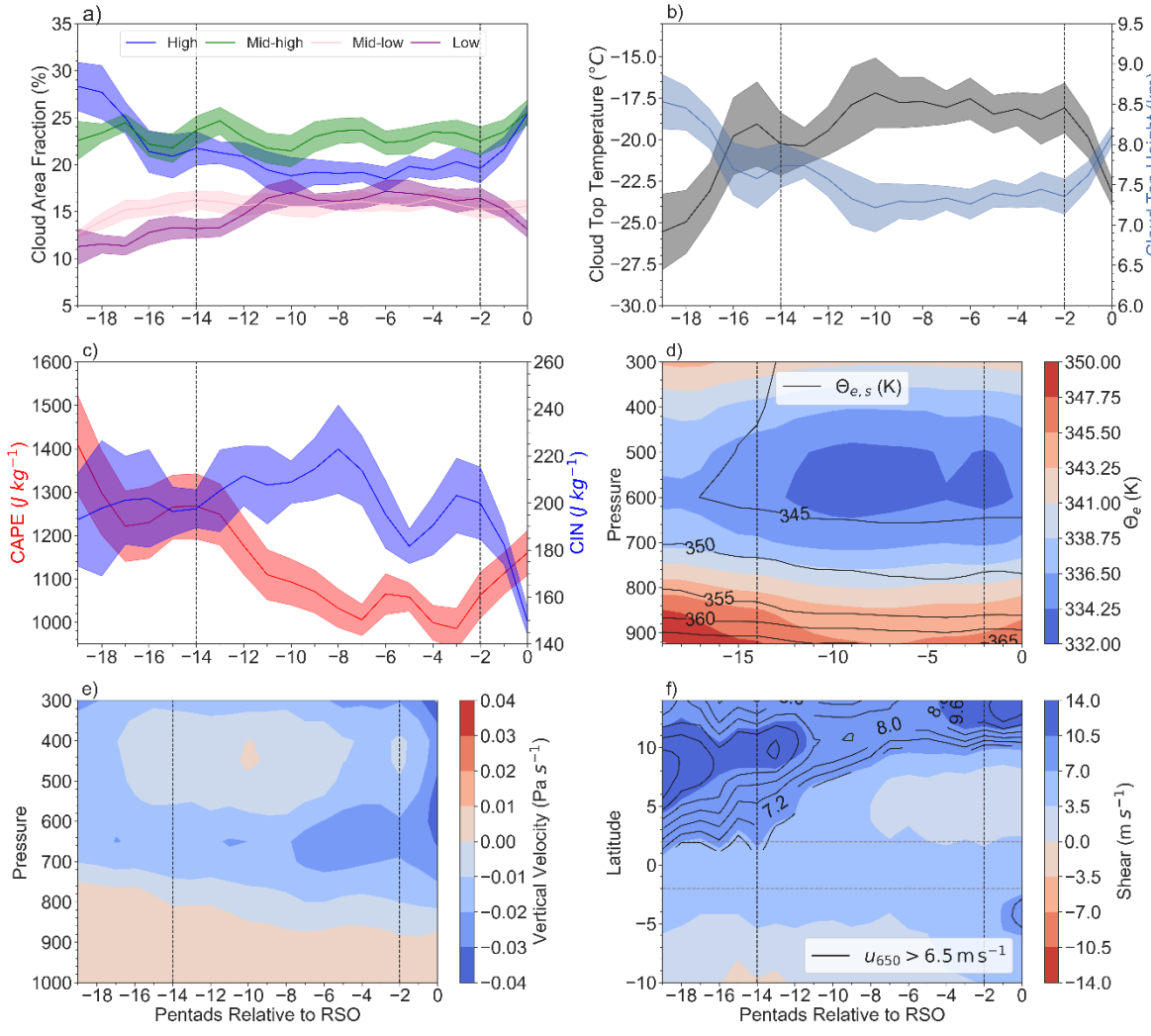

Figure 12: Prior to the fall RSO: (a) cloud area fraction for high, mid-high, mid-low, and low clouds; (b) cloud top temperature and cloud top height; (c) convective available potential energy; and convective inhibitive energy; (d)

https://doi.org/10.5194/egusphere-2025-4330
Preprint. Discussion started: 27 November 2025

equivalent potential temperature (θ_e; shades) and saturated equivalent potential temperature (θ_{e_s}); (e) vertical velocity; and (f) black contours: 650 hPa zonal wind greater than 6.5 m/s, denoting the AEJ-N. Shaded contours represent the wind shear ($u_{900} - u_{650}$). Shades of the time series in (a)- (c) represent the standard error of the mean of the different years. All the time series have been smoothed using a Savitsky-Golay filter (number of coefficients: 5, polynomial order 2).

Meanwhile, the contribution of ET to atmospheric moisture does not change significantly $f_{mix} = 0.612 \pm 0.082$ during the "before" period, while $f_{mix} = 0.665 \pm 0.168$ during the early transition (Fig. 11a, b). Therefore, it is the increases of low-level moisture from the Atlantic Ocean that initiate the early transition period prior to the fall RSO.

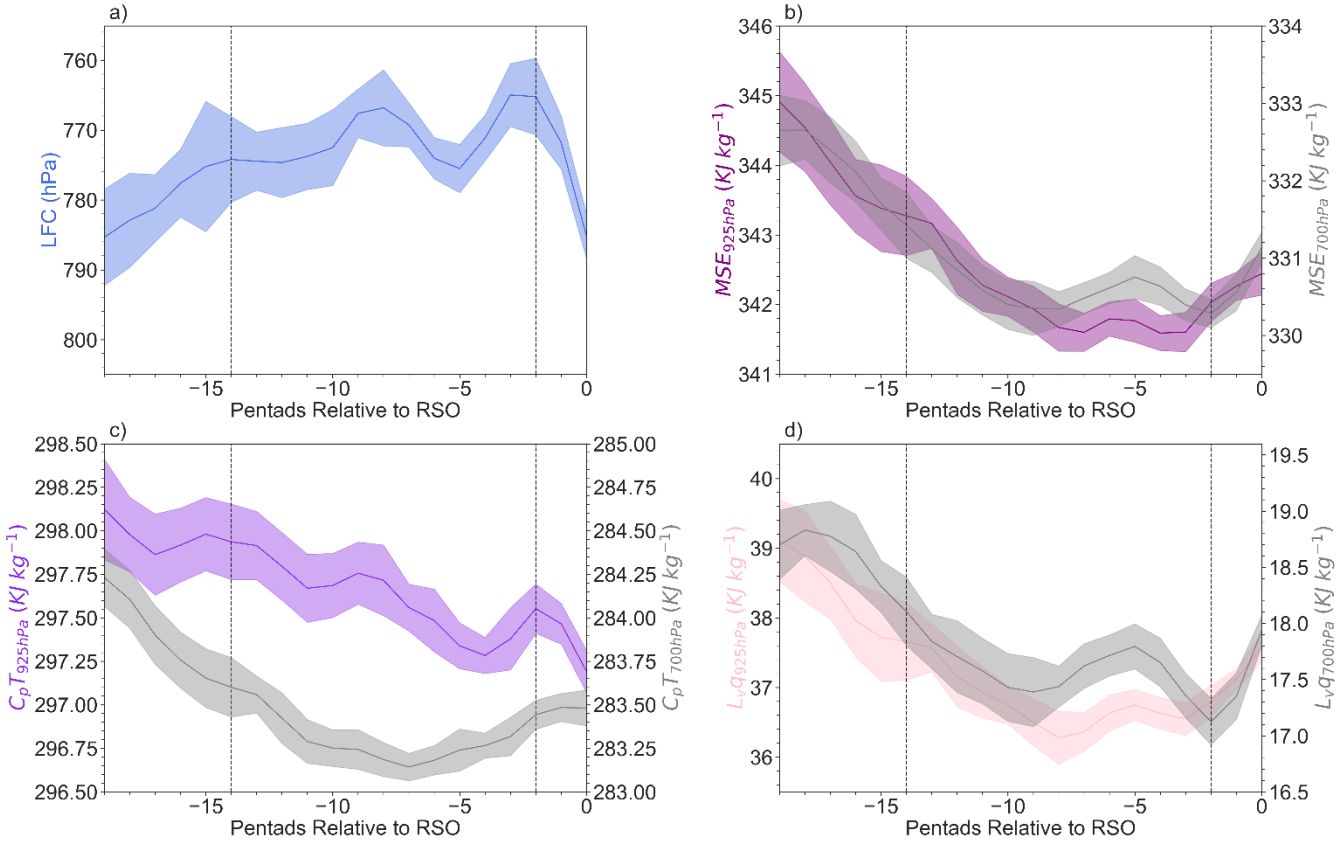

Figure 13: Evolution of (a) level of free convection (LFC), (b) MSE at 925 hPa and 700 hPa; (c) C_pT at 925 hPa and 700 hPa; and (d) L_vq at 925 hPa and 700 hPa. All are prior to the fall rainy season. All are averaged between $14E° - 26°E$ to account for effects of topography in the eastern part of the region. All have been smoothed using a Savitsky-Golay filter. Shades represents the standard error of the mean of the different years.

Despite an overall unstable lapse rate ($\frac{d\theta_e}{dp}$ <0), the thermodynamic condition of tropospheric column does not yet support deep convection. In the first half of the early transition, decreases in low-level atmospheric moisture (Fig. 13d) weakens negative $\frac{d\theta_e}{dp}$, coinciding with rising convective inhibitive energy and LFC, as well as decreasing convective available potential energy and low and mid-level MSE (Fig. 12c, d; Fig. 13b, c). Changes in MSE at both levels are mainly

https://doi.org/10.5194/egusphere-2025-4330
Preprint. Discussion started: 27 November 2025

due to changes in $L_v q$ rather than $C_p T$ (Fig. 13b, c, d). In the second half of the early transition, low-level moisture begins to increase, corresponding to increases in θ_e in the low-levels and strengthening negative (destabilizing) $\frac{d\theta_e}{dp}$ (Fig. 12c; Fig. 13d). This corresponds to the LFC stabilizing (no longer consistently increasing) between -7 to -2 pentads prior to the RSO (Fig. 13a) and decreases in convective inhibitive energy (Fig. 12c). Additionally, the vertical velocity is near zero above 600 hPa (Fig. 12e). Therefore, atmospheric dynamic conditions are not yet ready to facilitate increase of deep convection, consistent with relatively low and constant mid-high and high cloud covers (Fig. 12a), cloud top temperatures, and cloud top heights (Fig. 12b).

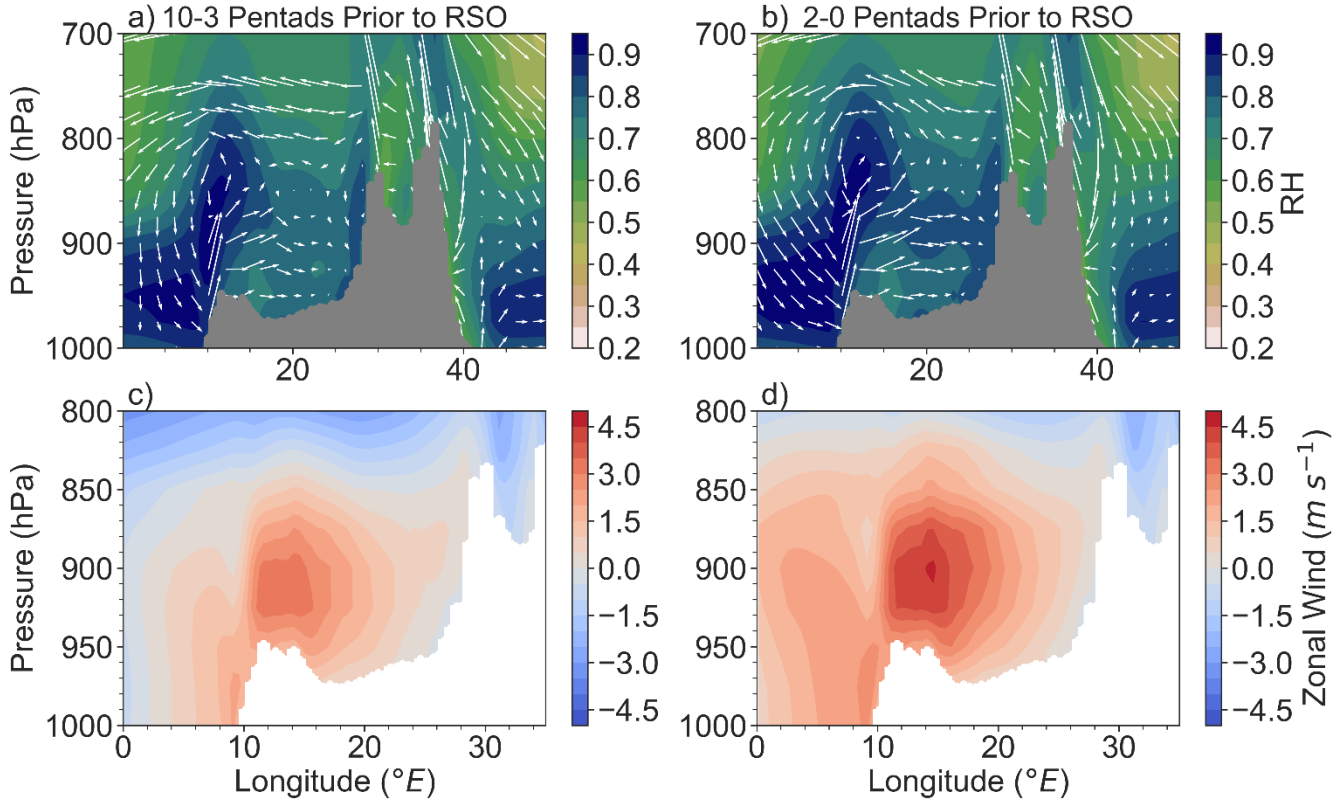

Figure 14: The zonal and vertical cross-section of relative humidity (shades) and vectors of u and ω averaged between 2°S-2°N for (a) the early transition period, i.e., 14-3 pentads prior to the fall RSO; (b) the late transition period, i.e., 2-0 pentads prior to the fall RSO. The vertical wind, ω, is magnified by multiple 100. As in (a)-(b), but for zonal wind speed (u) for (c) 14-3 pentads prior to the fall RSO; and d) 2-0 pentads prior to the fall RSO. Grey mask in (a)-(b) and white mask in (c)-(d) denote the topography of the region.

https://doi.org/10.5194/egusphere-2025-4330
Preprint. Discussion started: 27 November 2025

3.2.2 Late Transition Period

The late transition period to the fall rainy season starts with sharp increases in P, MF convergence, and CWV (Fig. 9a, b). Meanwhile, the contribution of ET to atmospheric moisture ($f = 0.613 \pm 0.194$) does not change significantly (Fig. 11c). Zonal MF convergence sharply increases, while meridional MF divergence weakens to near zero (Fig. 9c).

Zonally, the speed of low-level westerly wind that carry moisture from the Atlantic Ocean further increases (Fig. 10b,c). This is due to further increases in the zonal temperature gradient as the Atlantic cold tongue develops (Fig. S4b, c; Fig. S5; Caniaux et al., 2011), which increases the strength of the lower branch of the Congo Basin Cell (Longandjo and Rouault, 2020). Meanwhile, the strength of the mid-level zonal moisture transport does not change as much compared to its low-level counterpart, indicating that the sharp increase in net zonal MF convergence is driven by increases low-level moisture transport (Fig. 9c; Fig. B2a, b, e).

Meridionally, in the low-levels, moisture transport out of the southern boundary into the southern Congo continues to increase as the low-level winds move towards the Congo Air Boundary (Fig. 10b, c). However, this is compensated by moisture transport into the southern Congo across the southern boundary above 850 hPa (Fig. 10e, f, h, g; Fig. B2d). Across the northern boundary, low level moisture in the basin increases, acting against mid level moisture leaving the basin (Fig. B2c). Therefore, net meridional MF divergence decreases (Fig. 9c).

As the low-levels, atmospheric moisture increases rapidly due to increases in westerly winds (Fig. 14) and further destabilizes (strengthens negative $\frac{d\theta_e}{dp}$; Fig. 12d). The increased atmospheric moisture lifts up into the mid-troposphere above 800 hPa via the ascending branch of the Congo Basin Cell (located between $10°E - 20°C$) as well as orographically along the slope of the East African Rift (Fig. 14a, b), Therefore, mid-tropospheric relative humidity increases (Fig. 14b) despite subsidence in the low troposphere in the interior of the basin (Fig. 12e; Fig. 14b). As the mid-troposphere moistens, the thermodynamic atmospheric condition becomes favourable for deep convection rapidly, as shown by decreases in convective inhibitive energy (Fig. 12c) and LFC (Fig. 13a) and increases in convective available potential energy (Fig. 12c).

Meanwhile, despite the absence of the AEJ-N or AEJ-S over the equatorial region (Fig. 12f), the return branch of the Congo Basin Cell provides the vertical wind shear (Fig. 12f, on average within the equatorial region $8.30\ m\ s^{-1}$ during the late transition period prior to the fall RSO compared to $8.55\ m\ s^{-1}$ during the late transition period prior to the spring RSO) needed for favourable dynamic conditions for mesoscale convective systems (MCSs). These conditions enable rapid increase of P (Fig. 9a), and lead to the fall RSO as indicated by increases in the strength of vertical velocity from the lower atmosphere to 300 hPa (Fig. 12e), sharp increases (decreases) in high/mid-high (low) clouds, sharp increases in cloud top height, and sharp decreases in cloud top temperatures (Fig. 12a, b).

In summary, the transition from the boreal summer dry season to the fall RSO is mainly initiated by increasing westerly moisture transport from Atlantic Ocean into the equatorial Congo basin in the boundary layer via the lower branch of the Congo Basin Cell (925-875 hPa),. These changes start 14 pentads (around mid-June) before the fall RSO (around late August). This weakens the vertically integrated MF divergence, which, in turn, slows down the drying trend during the dry

https://doi.org/10.5194/egusphere-2025-4330
Preprint. Discussion started: 27 November 2025

season. Low-level moisture increases due to increases in moisture transport from the Atlantic Ocean during the early transition (14-3 pentads before the fall RSO). Mid-level atmospheric moisture increases as a result of increased uplift via the ascending branch of the Congo Basin Cell and orographic uplift against the East African Rift during the late transition period. This increases CWV, which subsequently reduces convective inhibitive energy and the LFC, while increasing convective available potential energy, MSE and vertical wind shear. Subsequently, the fall rainy season begins.

4 Discussion

4.1 Comparing the Transition to the Spring vs Fall Rainy Seasons

Here, we compare how conditions evolve to trigger the spring and fall rainy seasons, clarifying the similarities and differences in the controlling processes and their interactions that lead to each season's onset.

Prior to the spring rainy season, low-level moisture from the equatorial region is transported to the West African Heat Low, mixes with warm air from the Sahelian region (Fig. 4c; Fig. S1), uplifts, and then returns to the equatorial Congo (Fig. 4f) at the mid-levels (850-600 hPa). Therefore, a shallow meridional overturning cell exists that moves moisture northward at low levels, and southward at mid-levels. In contrast, prior to the fall rainy season, low-level moisture from the Atlantic Ocean turns towards the Congo Air Boundary located in the southern Congo. This low-level moisture transport into the equatorial Congo across the western boundary is greater in the fall rainy season compared to the spring rainy season, consistent with Pokam et al. (2012) who found that the Atlantic Ocean plays an important role in low-level moisture flux between August-November. As this low-level moisture reaches the Congo Air Boundary, it mixes with warm air from the southern Congo Basin (Fig. S4e, f) and South Africa (Worden and Fu 2025), uplifts, and then returns to the equatorial Congo (Fig. 10d-i) Therefore, a shallow meridional overturning cell exists that moves moisture southward at low levels, and northward at mid-levels.

Furthermore, the Congo Basin Cell moves further into the interior of the basin prior to the fall RSO compared to the spring RSO, with its ascending branch located around $20°E$ prior to the fall and located around $15°E$ prior to the spring rainy season (Fig. 8a, b; Fig. 14a, b). Therefore, less moisture is brought into the region across its western boundary prior to the spring (Fig. B1a; Fig. B2a). Finally, the cause of the lower to middle tropospheric wind shear differs between the two rainy seasons. The zonal shear increases prior to the start of the rainy season is induced by the formation of the AEJ-N, present in the equatorial region. Meanwhile, prior to the fall rainy season, shear exists due to the return branch of the Congo Basin Cell, at similar pressure levels, but it is weaker compared to the wind shear prior to the spring RSO.

Additionally, the thermodynamic conditions are more favourable for convection prior to the fall RSO than the spring RSO. Convective inhibitive energy prior to the spring rainy season ranges from 226-308 J/Kg and is 226 J/kg 1 pentad prior to RSO, while convective inhibitive energy prior to the fall rainy season ranges from 149-222 J/kg and is at 149 J/kg 1 pentad prior to the RSO. The LFC is also higher by the beginning of the spring RSO compared to the fall RSO.

https://doi.org/10.5194/egusphere-2025-4330
Preprint. Discussion started: 27 November 2025

Therefore, the cloud base is higher, and convective air must overcome stronger convective inhibitive energy prior to the spring RSO.

Finally, both transition periods show increasing low-level atmospheric moisture before increases in mid-level atmosphere, and the moistening of the mid-level during late transition seasons that is important for increasing deep convection and initiating both RSOs. The increase of low-level zonal moisture transport is mainly responsible for increasing the lower-level moisture, whereas the increase of mid-level is main due to lifting of the low-level moisture to the mid-level by ascending branch of the Congo Basin Cell over the western equatorial Congo basin and by the East African rift over the eastern equatorial Congo basin.

4.2 Comparing the Transition to the Fall Rainy Season in the Equatorial vs Southern Congo

We next compare the transition period to the fall rainy season in the equatorial versus southern Congo. The fall rainy season onset is earlier over the equatorial Congo basin, beginning on average 29 August, than that over the southern Congo, beginning on average 9 October (Worden and Fu, 2025). This difference in timing is likely driven, in part, by the seasonal movement of the Congo Air Boundary (Longandjo and Rouault, 2020), which is centred closer to the equator prior to the equatorial RSO (Fig. 10b, c) and then moves towards the southern Congo prior to the fall RSO (Worden and Fu, 2025). This southward movement brings with it moisture from the equatorial region, supporting the southern Congo RSO in boreal fall. Furthermore, moisture contributions between the two regions differ greatly. ET is the dominant contributor to atmospheric moisture prior to the fall rainy season in the equator; however, it does not change significantly during the transition period. Meanwhile, for the southern region, ET increases significantly and contributes equally to atmospheric moisture as the oceanic moisture transport by the late transition period. Therefore, the increases of moisture prior to the RSOs in the equatorial region are primarily controlled by advected oceanic moisture, while over the southern Congo, moisture increases are controlled by increases of both moisture transport from the ocean and from ET over land.

Additionally, atmospheric instability differs strongly. In the equatorial region, convective available potential energy is much higher than convective inhibitive energy for the entire transition period, helping initiate a large jump in P once convective inhibitive energy decreases as there is plenty of energy for deep convection. However, in the southern region, convective available potential energy is lower, and convective inhibitive energy is higher than in the equatorial Congo, where above 700 hPa is dominated by adiabatic warming due to subsidence until the late transition period. Therefore, the equatorial region has larger potential for storms and heavy rain to occur than in the southern Congo basin.

Finally, the AEJs play different roles between the equatorial region and the southern Congo. In the equatorial region, both the AEJ-S and AEJ-N do not play a direct role in determining vertical wind shear prior to the fall RSO. In contrast, the AEJ-S directly contributes to the vertical wind shear prior to the RSO in the southern Congo. Therefore, it is important to consider the sub-basin scale variability in the evolution of atmospheric conditions prior to the transition to the RSOs that will likely react differently to climate perturbations and hence the seasonal rainfall cycle.

https://doi.org/10.5194/egusphere-2025-4330
Preprint. Discussion started: 27 November 2025

5 Conclusion

Using a suite of satellite and reanalysis data, we examined the mechanisms controlling the transition periods to the spring and fall rainy season in the equatorial Congo. We summarize these mechanisms below.

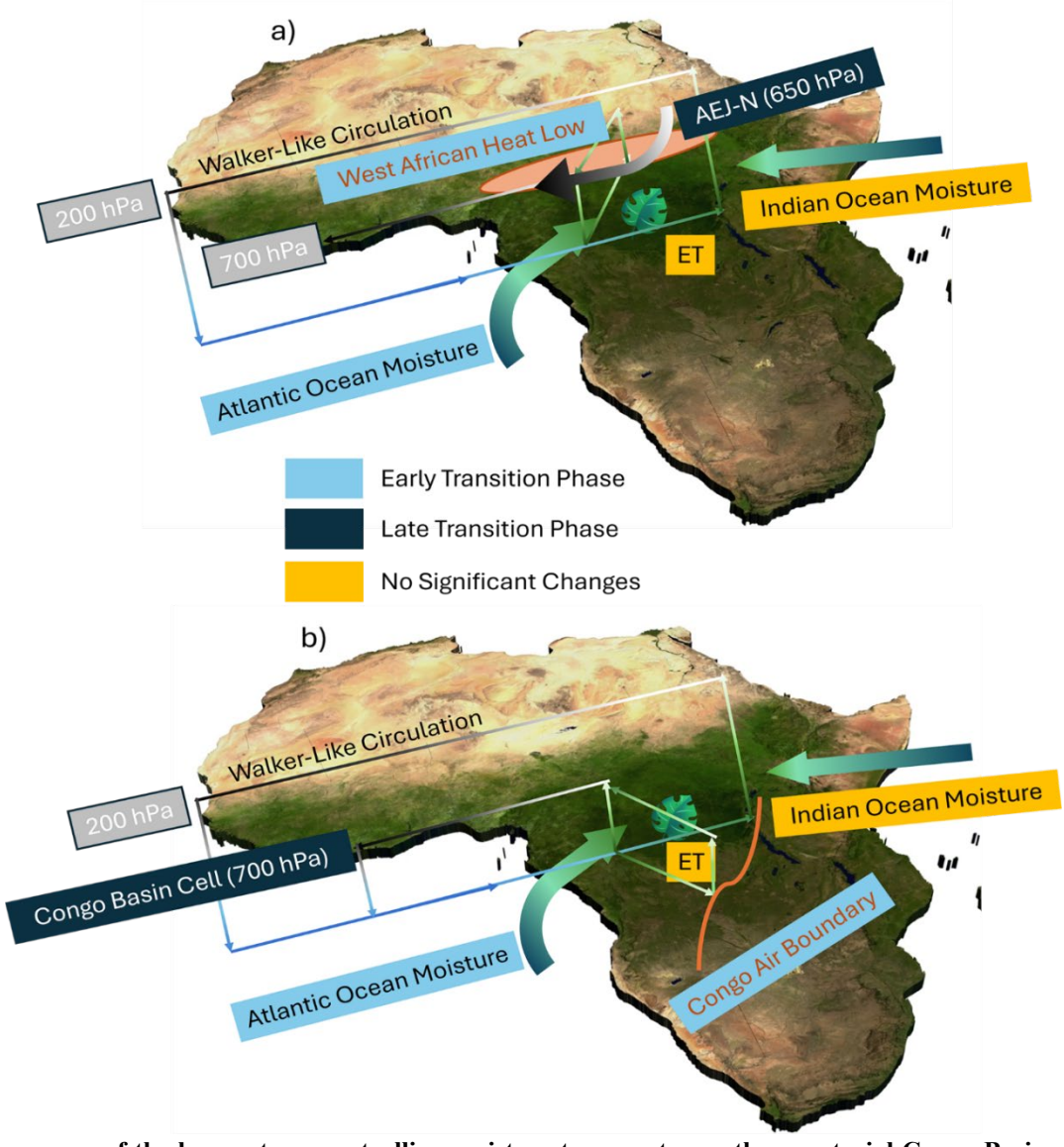

Figure 15: Summary of the key systems controlling moisture transport over the equatorial Congo Basin prior to (a) the spring RSO and (b) the fall RSO.

Spring rainy season onset:

(1) *Early-transition:* This period starts with a turning point from strengthening to weakening of the vertically integrated MF divergence. Changes in both zonal and meridional MF lead to near zero vertically integrated MF divergence by the end

https://doi.org/10.5194/egusphere-2025-4330
Preprint. Discussion started: 27 November 2025

of this period. This is due to (1) increases in low-level moisture entering the basin from the Atlantic Ocean; and (2) initial decreases and then increases in mid-level moisture entering the basin from the Indian Ocean and leaving the basin back towards the Atlantic Ocean. Changes in net meridional MF are due to increases in low-level moisture leaving the basin across the northern boundary towards the West African heat low level moisture entering the basin across the southern boundary. ET contributes the most to atmospheric moisture but does not change significantly. Meanwhile, large convective available potential energy, and negative $\frac{d\theta_e}{dp}$,but large convective inhibitive energy and high LFC, as well as the presence of subsidence in the upper troposphere, indicates that thermodynamic conditions are beginning to change in favour of deep convection.

(2) *Late-transition:* This period starts with increases sharp increases in CWV, indicating atmospheric moistening, MF convergence, and P. Increases in low-level moisture transport into the region from the Atlantic Ocean and mid-level transport into the region from the Indian Ocean act against moisture leaving the region at mid-levels back towards the Atlantic Ocean. Low-level moisture is lifted to the mid-troposphere by the ascending branch of the Congo Basin Cell on the western edge of the region, and by orographic uplift in the eastern part of the region as moisture is pushed up the East African Rift. At the mid-levels, meridional MF convergence strengthens: more moisture transport enters the region across the northern boundary than leaves the basin across the southern boundary. Therefore, mid-level atmospheric moisture increases, causing decreases in convective inhibitive energy and lowering of the LFC. Additionally, the AEJ-N forms, providing vertical wind shear. This all leads to sharp increases in P. That ET contribution to atmospheric moisture does not change significantly indicates that it provides background moisture but does not contribute to transitioning the atmospheric conditions to be conducive for deep convection.

Fall rainy season onset:

(1) Early Transition: This period starts from a turning point from increasing to weakening vertically integrated MF divergence, which reaches convergence about halfway through the period. These changes are primarily due to large increases in net zonal MF convergence, as increases in low-level moisture transport from the Atlantic Ocean, due to the strengthening of the low-branch Congo Basin Cell (Longandjo and Rouault, 2020), act against mid-level moisture transport out of the region back towards the Atlantic Ocean. Therefore, low-level moisture increases in the second half of the transition period, increasing CWV and strengthening the negative $\frac{d\theta_e}{dp}$ gradient. However, as mid-level atmospheric moisture decreases to a minimum, atmospheric thermodynamic conditions are not yet ready to support deep convection, as convective inhibitive energy and the LFC are high.

(2) Late Transition: CWV, MF convergence, and P increase sharply. ET remains the same, but it contributes an equal amount of atmospheric moisture for rainfall as in the early transition period. Net zonal MF convergence increases as low-level moisture from the Atlantic Ocean increases. Net meridional MF divergence goes to near zero despite increases in low-level moisture transport towards the Congo Air Boundary across the southern boundary. Low-level moisture is pushed upwards by the ascending branch of the Congo Basin Cell, located more centrally in the region compared to

https://doi.org/10.5194/egusphere-2025-4330
Preprint. Discussion started: 27 November 2025

prior to the spring RSO, as well as up against the East African Rift. This, along with increases in net mid-level meridional moisture transport convergence (moisture transport entering the basin is greater than moisture transport leaving the basin above 850 hPa) moistens the mid-troposphere, lowering convective inhibitive energy and the LFC. The westerly return branch of the Congo Basin Cell provides the vertical shear needed. Therefore, conditions are conducive for the start of the rainy season.

The clarification of the atmospheric processes that drive the dry to rainy season transition provided by this study will lay the groundwork for understanding variability in the seasonal cycle of precipitation. This includes changes induced by ENSO, the Indian Ocean Dipole, and Madden-Julian Oscillations (e.g., Kebacho and Sarfo, 2023; Moihamette et al., 2022; Jury et al., 2009; Creese et al., 2019), variability induced by aerosols (Chakraborty et al., 2020), by the poleward movement of the northern and southern heat lows (Cook et al., 2020), and by the long-term AMJ drought (Jiang et al., 2019). Overall, the equatorial region seasonal rainfall is influenced by a combination of local (e.g., ET providing background moisture, and orographic uplift) and regional factors (e.g., moisture from the Atlantic Ocean, the West African Heat Low, and the Congo Air Boundary). Therefore, it is important to consider the influence of climate variability on the rainy season timing and intensity on both scales.

6 Appendices

6.1 Appendix A

The following text further explains the comparison of the observed δD measurements to the mixing and Rayleigh models, as well as the error calculations involved:

A mixing model is described as follows:

$$\delta_{mix} = q_0(\delta_0 - \delta_F)\frac{1}{q} + \delta_F \quad \text{Eq. A1}$$

Where q_0 and δ_o are, respectively, the specific humidity and its δD value of the dry air mass in the upper troposphere, and q_F and δ_F are, respectively, the specific humidity and δD value of the air mass at the surface. $q = q_0 + q_F$ is the specific humidity of the mixed air mass between dry air mass in the upper troposphere and humid air mass from its surface source (Noone, 2012).

We also examine the observed δD values in relation to a Rayleigh model, which describes the change of δD with water vapor mixing rate as liquid water evaporates in equilibrium with temperature:

$$\delta_{ray} \simeq (\alpha - 1)\ln\left(\frac{q}{q_0}\right) + \delta_0 \quad \text{Eq. A2}$$

where α is set to equal the temperature-dependent equilibrium fractionation factor between liquid and water vapor (Majoube, 1971). Further discussion of δD and these models can be found in (Worden et al., 2021).

https://doi.org/10.5194/egusphere-2025-4330
Preprint. Discussion started: 27 November 2025

Following Worden et al. (2021), we compare the observed δD measurements to the mixing and Rayleigh models to identify the relative contribution of ET to atmospheric moisture. The initial values of modeled δD (δ_F) were $-50‰$ and $-80‰$ for land-based and ocean-based models, respectively, chosen based on representative values of δD from land and ocean. Any observed δD above the land-based mixing model is considered as transpired by the plants over land. Any δD value shown between the land-based and ocean-based mixing models likely comes from some mixture of the two sources. The fraction of atmospheric moisture coming from ET is represented by the fraction of observed δD above the land-based mixing model (f_{mix}). This fraction can be considered a lower bound on the amount of ET contributing to atmospheric moisture because rainfall processes as well as vapor originating from oceans or evaporation and mixing with vapor from ET will decrease δD. To calculate the error on this fraction, we assume a 12‰ error in the δD observations, and recalculate the fraction of δD above the land-based mixing model with 12‰ added and subtracted from the observations as in Worden et al. (2021). We then find the differences between the original fraction and the new fractions and average the two to calculate our final error.

6.2 Appendix B

https://doi.org/10.5194/egusphere-2025-4330
Preprint. Discussion started: 27 November 2025

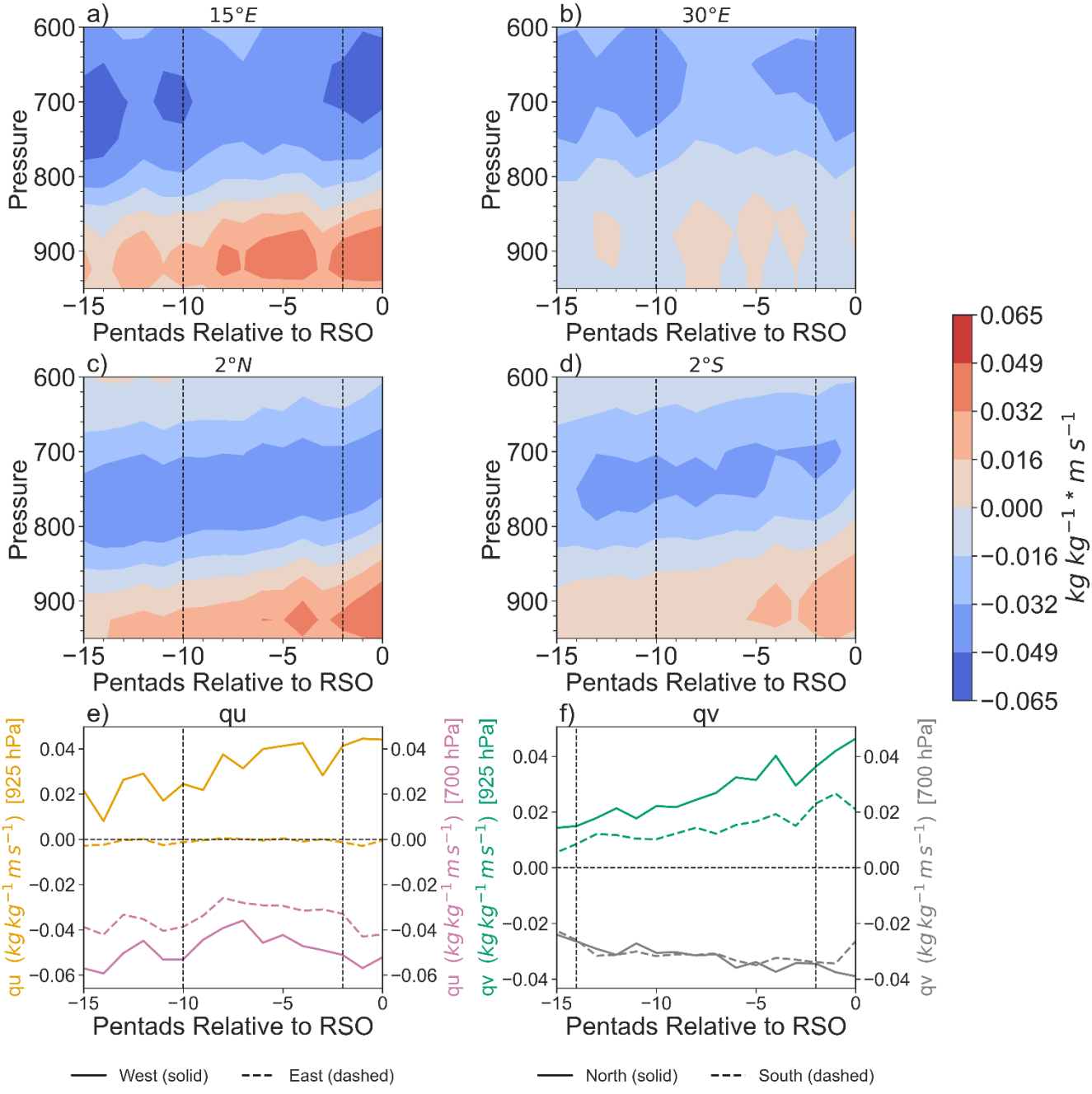

Figure B1: (a) Zonal moisture transport ($q * u$) across $15°E$ and between $2°S - 2°N$; (b) zonal moisture transport ($q * v$) across $30°E$ and between $2°S - 2°N$. Note that contours below 875 hPa should not be considered as they are below the East African Rift, but all pressure levels are shown to emphasize the mid-level moisture transport. (c) meridional moisture transport ($q * v$) across $2°N$ and between $15°E - 30°E$; d) meridional moisture transport ($q * v$) across $2°S$ and between $15°E - 30°E$; e) zonal moisture transport at 925 hPa (orange) and 700 hPa (purple)

https://doi.org/10.5194/egusphere-2025-4330
Preprint. Discussion started: 27 November 2025

across the western and eastern boundaries; and f) meridional moisture transport at 925 hPa (green) and 700 hPa (grey) cross the northern and southern boundaries. For (a) and (b), positive values equal eastward transport and negative equal westward transport. For (c) and (d), positive equals northward transport and negative values equal southward transport. Additionally, for longitude values greater than $26°E$, meridional moisture transport values have been masked out between 925-875 hPa to account for the topography of the East African Rift. Therefore, shades below 875 hPa represent meridional moisture transport between $15°E - 26°E$. Prior to the spring RSO.

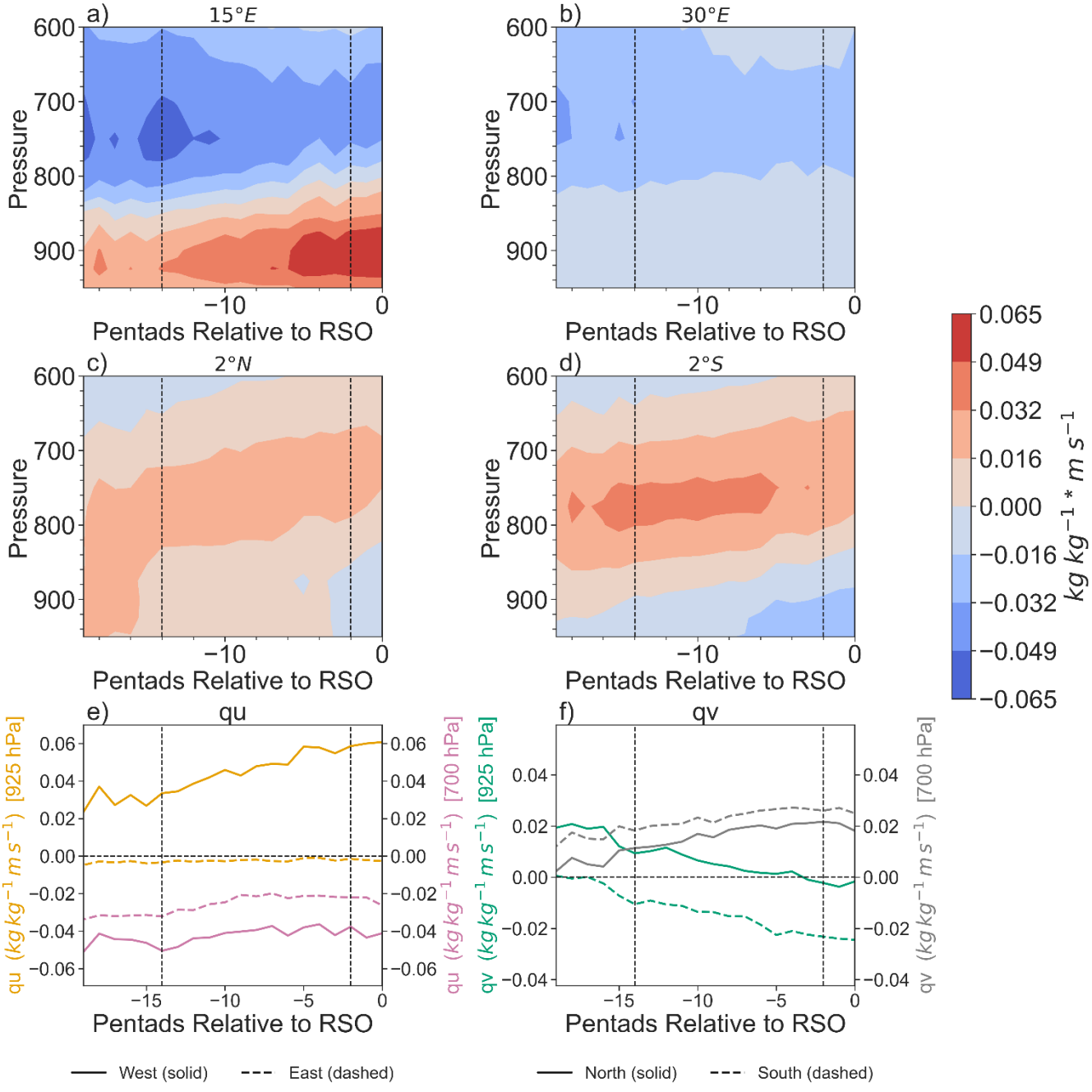

https://doi.org/10.5194/egusphere-2025-4330
Preprint. Discussion started: 27 November 2025

Figure B2: a) zonal moisture transport ($q * u$) across $15°E$ and between $2°S - 2°N$; b) zonal moisture transport ($q * v$) across $30°E$ and between $2°S - 2°N$. Note that contours below 875 hPa should not be considered as they are below the East African Rift, but all pressure levels are shown to emphasize the mid-level moisture transport. c) meridional moisture transport ($q * v$) across $2°N$ and between $15°E - 30°E$; and d) meridional moisture transport ($q * v$) across $2°S$ and between $15°E - 30°E$; e) zonal moisture transport at 925 hPa (orange) and 700 hPa (purple) across the western and eastern boundaries; and f) meridional moisture transport at 925 hPa (green) and 700 hPa (grey) cross the northern and southern boundaries. For a) and b), positive values equal eastward transport and negative values equal westward transport. For c) and d), positive values equal northward transport and negative values equals southward transport. Additionally, for longitude values greater than $26°E$, meridional moisture transport values have been masked out between 925-875 hPa to account for the topography of the East African Rift. Therefore, shades below 875 hPa represent meridional moisture transport between $15°E - 26°E$. Prior to the fall RSO.

7 Code Availability

Code can be made available by request to the corresponding author (Sarah Worden, sarah.r.worden@jpl.nasa.gov)

8 Data Availability

GLEAM evapotranspiration estimates can be downloaded via the GLEAM website: https://www.gleam.eu/. Version 3.7b can be made available by request to the corresponding author Sarah Worden (sarah.r.worden@jpl.nasa.gov). All AIRS TqJoint data and TRMM 3b42 daily precipitation can be downloaded using the NASA GES DISC: https://disc.gsfc.nasa.gov. ERA5 products can be found at: https://cds.climate.copernicus.eu/cdsapp#!/home. TES HDO and H2O estimates can be found at: https://catalog.data.gov/dataset/tes-aura-l2-hdo-limb-v006. CERES cloud and products can be found at: https://ceres-tool.larc.nasa.gov/ord-tool/jsp/SYN1degEd41Selection.jsp

9 Author Contribution

All authors contributed to the study conception and design. S.W. performed experimental design, data collection, analysis, and manuscript writing. R.F. performed experimental design and manuscript writing. All authors read and approved the final manuscript.

10 Competing Interests

The authors declare that they have no conflict of interest.

11 Acknowledgments

Part of this research was carried out at the Jet Propulsion Laboratory, California Institute of Technology, under a contract with the National Aeronautics and Space Administration (80NM0018D0004).

https://doi.org/10.5194/egusphere-2025-4330
Preprint. Discussion started: 27 November 2025

12 Financial Support

This work was supported by the NASA FINNEST grant #80NSSC20K1654 and NSF Grant Number 1917781.

13 References

Alsdorf, D., Beighley, E., Laraque, A., Lee, H., Tshimanga, R., O'Loughlin, F., et al. (2016). Opportunities for hydrologic research in the Congo Basin. Reviews of Geophysics, 54(2), 378–409. https://doi.org/10.1002/2016RG000517

Attwood, K., Washington, R., & Munday, C. (2024). The Southern African Heat Low: Structure, Seasonal and Diurnal Variability, and Climatological Trends. Journal of Climate. https://doi.org/10.1175/JCLI-D-23-0522.1

Aumann, H. H., Broberg, S., Manning, E., & Pagano, T. (2019). Radiometric Stability Validation of 17 Years of AIRS Data Using Sea Surface Temperatures. Geophysical Research Letters, 46, 12504– 12510. https://doi.org/10.1029/2019GL085098.

Balas, N., Nicholson, S. E., & Klotter, D. (2007). The relationship of rainfall variability in West Central Africa to sea-surface temperature fluctuations. International Journal of Climatology, 27(10), 1335–1349. https://doi.org/10.1002/joc.1456

Bolton, D. (1980). The computation of equivalent potential temperature. Monthly weather review, 108(7), 1046-1053. https://doi.org/10.1175/1520-0493(1980)108<1046:TCOEPT>2.0.CO;2

Bretherton, C. S., Peters, M. E., & Back, L. E. (2004). Relationships between water vapor path and precipitation over the tropical oceans. Journal of Climate, 17(7), 1517–1528. https://doi.org/10.1175/1520-0442(2004)017<1517:RBWVPA>2.0.CO;2

Brummett, R.E., C. Tanania, A. Pandi, J. Ladel, Y. Munzimi, A. Russell, et al. (2009). Ressources en eau et biens et services liés à l'écosystème forestier. In: Wasseige, C., Devers, D., de Marcen, P., Eba'a Atyi, R., Nasi, R., & Mayaux, P. (Eds.) Les forêts du Bassin du Congo. Office des publications de l'Union européenne, Luxembourg. 10.2788/32456.

Caniaux, G., Giordani, H., Redelsperger, J. L., Guichard, F., Key, E., & Wade, M. (2011). Coupling between the Atlantic cold tongue and the West African monsoon in boreal spring and summer. Journal of Geophysical Research: Oceans, 116(C4). https://doi.org/10.1029/2010JC006570

Chakraborty, S., Jiang, J. H., Su, H., & Fu, R. (2020). Deep convective evolution from shallow clouds over the Amazon and Congo rainforests. Journal of Geophysical Research: Atmospheres, 125(1), e2019JD030962. https://doi.org/10.1029/2019JD030962

Chakraborty, S., Jiang, J. H., Su, H., & Fu, R. (2021). On the role of aerosol radiative effect in the wet season onset timing over the Congo rainforest during boreal autumn. Atmospheric Chemistry and Physics, 21(17), 12855-12866. https://doi.org/10.5194/acp-21-12855-2021.

Chen, T. C. (2005). Maintenance of the midtropospheric North African summer circulation: Saharan high and African easterly jet. Journal of climate, 18(15), 2943-2962. https://doi.org/10.1175/JCLI3446.1

Cook, K. H., Liu, Y., & Vizy, E. K. (2020). Congo Basin drying associated with poleward shifts of the African thermal lows. Climate Dynamics, 54, 863-883. https://doi.org/10.1007/s00382-019-05033-3

https://doi.org/10.5194/egusphere-2025-4330
Preprint. Discussion started: 27 November 2025

Cook, K. H., & Vizy, E. K. (2016). The Congo Basin Walker circulation: Dynamics and connections to precipitation. Climate Dynamics, 47(3–4), 697–717. https://doi.org/10.1007/s00382-015-2864-y

Cook, K. H., & Vizy, E. K. (2022). Hydrodynamics of regional and seasonal variations in Congo Basin precipitation. Climate Dynamics, 59(5-6), 1775-1797. https://doi.org/10.1007/s00382-021-06066-3
Creese, A., Washington, R., & Jones, R. (2019). Climate change in the Congo Basin: processes related to wetting in the December–February dry season. Climate Dynamics, 53, 3583-3602. https://doi.org/10.1007/s00382-019-04728-x

Cook, K. H., Liu, Y., & Vizy, E. K. (2020). Congo Basin drying associated with poleward shifts of the African thermal lows. Climate Dynamics, 54(1), 863-883. https://doi.org/10.1007/s00382-019-05033-3

DeSouza-Machado, S., Strow, L. L., Tangborn, A., Huang, X., Chen, X., Liu, X., Wu, W., and Yang, Q. (2018). Single-footprint retrievals for AIRS using a fast TwoSlab cloud-representation model and the SARTA all-sky infrared radiative transfer algorithm. Atmos. Meas. Tech., 11, 529–550. https://doi.org/10.5194/amt-11-529-2018

Doelling, D. R., N. G. Loeb, D. F. Keyes, M. L. Nordeen, D. Morstad, C. Nguyen, B. A. Wielicki, D. F. Young, M. Sun. (2013). Geostationary Enhanced Temporal Interpolation for CERES Flux Products, Journal of Atmospheric and Oceanic Technology, **30**(6), 1072-1090. doi: 10.1175/JTECH-D-12-00136.1.

Doelling, D. R., M. Sun, L. T. Nguyen, M. L. Nordeen, C. O. Haney, D. F. Keyes, P. E. Mlynczak. (2016). Advances in Geostationary-Derived Longwave Fluxes for the CERES Synoptic (SYN1deg) Product, Journal of Atmospheric and Oceanic Technology, 33(3), 503-521. doi: 10.1175/JTECH-D-15-0147.1

Galewsky, J. (2018). Using stable isotopes in water vapor to diagnose relationships between lower-tropospheric stability, mixing, and low-cloud cover near the island of Hawaii. Geophysical Research Letters, 45(1), 297–305. https://doi.org/10.1002/2017GL075770

Galewsky, J., & Hurley, J. V. (2010). An advection-condensation model for subtropical water vapor isotopic ratios. Journal of Geophysical Research, 115(D16), D16116. https://doi.org/10.1029/2009JD013651

Hart, N. C., Washington, R., & Maidment, R. I. (2019). Deep convection over Africa: Annual cycle, ENSO, and trends in the hotspots. Journal of Climate, 32(24), 8791-8811. https://doi.org/10.1175/JCLI-D-19-0274.1

Hersbach, H., Bell, B., Berrisford, P., Hirahara, S., Horányi, A., Muñoz-Sabater, J., et al. (2020). The ERA5 global reanalysis. Quarterly Journal of the Royal Meteorological Society, 146(730), 1999–2049. https://doi.org/10.1002/QJ.3803

Hua, W., Zhou, L., Chen, H., Nicholson, S. E., Raghavendra, A., & Jiang, Y. (2016). Possible causes of the Central Equatorial African long-term drought. Environmental Research Letters, 11(12). https://doi.org/10.1088/1748-9326/11/12/124002

Hosking, J. S., Russo, M. R., Braesicke, P., & Pyle, J. A. (2010). Modelling deep convection and its impacts on the tropical tropopause layer. Atmospheric Chemistry and Physics, 10(22), 11175-11188. https://doi.org/10.5194/acp-10-11175-2010

Howard, E., & Washington, R. (2018). Characterizing the synoptic expression of the Angola low. Journal of Climate, 31(17), 7147-7165. https://doi.org/10.1175/JCLI-D-18-0017.1

Howard, E., & Washington, R. (2019). Drylines in southern Africa: Rediscovering the Congo air boundary. Journal of Climate, 32(23), 8223-8242. https://doi.org/10.1175/JCLI-D-19-0437.1

https://doi.org/10.5194/egusphere-2025-4330
Preprint. Discussion started: 27 November 2025

Hua, W., Zhou, L., Nicholson, S. E., Chen, H., & Qin, M. (2019). Assessing reanalysis data for understanding rainfall climatology and variability over Central Equatorial Africa. Climate Dynamics, 53(1–2), 651–669. https://doi.org/10.1007/s00382-018-04604-0

Huffman, G. J., Bolvin, D. T., Nelkin, E. J., Wolff, D. B., Adler, R. F., Gu, G., et al. (2007). The TRMM multisatellite precipitation analysis (TMPA): Quasi-global, multiyear, combined-sensor precipitation estimates at fine scales. Journal of Hydrometeorology, 8(1), 38–55. https://doi.org/10.1175/JHM560.1

Irion, F. W., Kahn, B. H., Schreier, M. M., Fetzer, E. J., Fishbein, E., Fu, D., Kalmus, P., Wilson, R. C., Wong, S., and Yue, Q. (2018). Single-footprint retrievals of temperature, water vapor and cloud properties from AIRS,.Atmos. Meas. Tech., 11, 971–995. https://doi.org/10.5194/amt-11-971-2018.

Jiang, Y., Zhou, L., Tucker, C. J., Raghavendra, A., Hua, W., Liu, Y. Y., & Joiner, J. (2019). Widespread increase of boreal summer dry season length over the Congo rainforest. Nature Climate Change, 9, 617–622. https://doi.org/10.1038/s41558-019-0512-y

Jury, M. R., Matari, E., & Matitu, M. (2009). Equatorial African climate teleconnections. Theoretical and applied climatology, 95, 407-416. https://doi.org/10.1007/s00704-008-0018-4

Kebacho, L. L., & Sarfo, I. (2023). Why Eastern Africa was not dry during the 2020 short rainy season despite La Niña and a negative Indian Ocean Dipole: Interplay between the Madden-Julian Oscillation and La Niña in modulating short rain. Theoretical and Applied Climatology, 153(3), 1191-1201. https://doi.org/10.1007/s00704-023-04519-9

Kuete, G., Pokam Mba, W., & Washington, R. (2020). African Easterly Jet South: control, maintenance mechanisms and link with Southern subtropical waves. Climate Dynamics, 54(3-4), 1539-1552. https://doi.org/10.1007/s00382-019-05072-w

Lacour, J.-L., Risi, C., Worden, J., Clerbaux, C., & Coheur, P.-F. (2018). Importance of depth and intensity of convection on the isotopic composition of water vapor as seen from IASI and TES δ D observations. Earth and Planetary Science Letters, 481, 387–394. https://doi.org/10.1016/j.epsl.2017.10.048

Lavaysse, C., Flamant, C., Janicot, S., Parker, D. J., Lafore, J. P., Sultan, B., & Pelon, J. (2009). Seasonal evolution of the West African heat low: a climatological perspective. Climate Dynamics, 33, 313-330. https://doi.org/10.1007/s00382-009-0553-4.

Li, W., & Fu, R. (2004). Transition of the large-scale atmospheric and land surface conditions from the dry to the wet season over Amazonia as diagnosed by the ECMWF re-analysis. Journal of Climate, 17(13), 2637-2651. https://doi.org/10.1175/1520-0442(2004)017<2637:TOTLAA>2.0.CO;2

Longandjo, G. N. T., and Rouault, M. (2020). "On the Structure of the Regional-Scale Circulation over Central Africa: Seasonal Evolution, Variability, and Mechanisms". Journal of Climate 33.1, 145-162. https://doi.org/10.1175/JCLI-D-19-0176.1

Longandjo, G. N. T., & Rouault, M. (2023). Revisiting the Seasonal Cycle of Rainfall over Central Africa. Journal of Climate. https://doi.org/10.1175/JCLI-D-23-0281.1

Majoube, M. (1971). Fractionnement en oxygène 18 et en deutérium entre l'eau et sa vapeur. Journal de Chimie Physique, 68, 1423–1436. https://doi.org/10.1051/jcp/1971681423

https://doi.org/10.5194/egusphere-2025-4330
Preprint. Discussion started: 27 November 2025

Martens, B., Miralles, D. G., Lievens, H., van der Schalie, R., de Jeu, R. A. M., Fernández-Prieto, D., et al. (2017). GLEAM v3: satellite-based land evaporation and root-zone soil moisture. Geosci. Model Dev., 10, 1903–1925. https://doi.org/10.5194/gmd-10-1903-2017.

Mba, W.P., Vondou, D.A. & Kamsu-Tamo, P.H. (2022). Central African Climate. In Congo Basin Hydrology, Climate, and Biogeochemistry (eds R.M. Tshimanga, G.D.M. N'kaya and D. Alsdorf). https://doi.org/10.1002/9781119657002.ch2.

Moihamette, F., Pokam, W. M., Diallo, I., & Washington, R. (2022). Extreme Indian Ocean dipole and rainfall variability over Central Africa. International Journal of Climatology, 42(10), 5255-5272. https://doi.org/10.1002/joc.7531

Neupane, N. (2016). The Congo Basin zonal overturning circulation. Adv. Atmos. Sci., 33, 767–782, https://doi.org/10.1007/s00376-015-5190-8.

Nicholson, S. E. (2018). The ITCZ and the seasonal cycle over equatorial Africa. Bulletin of the American Meteorological Society, 99(2), 337–348. https://doi.org/10.1175/BAMS-D-16-0287.1

Nicholson, S.E. (2022). The Rainfall and Convective Regime over Equatorial Africa, with Emphasis on the Congo Basin. In Congo Basin Hydrology, Climate, and Biogeochemistry (eds R.M. Tshimanga, G.D.M. N'kaya and D. Alsdorf). https://doi.org/10.1002/9781119657002.ch3.

Nicholson, S. E., & Dezfuli, A. K. (2013). The relationship of rainfall variability in western equatorial Africa to the tropical oceans and atmospheric circulation. Part I: The boreal spring. Journal of Climate, 26(1), 45–65. https://doi.org/10.1175/JCLI-D-11-00653.1

Nicholson, S. E., & Grist, J. P. (2003). The seasonal evolution of the atmospheric circulation over West Africa and equatorial Africa. Journal of climate, 16(7), 1013-1030. https://doi.org/10.1175/1520-0442(2003)016<1013:TSEOTA>2.0.CO;2

Noone, D. (2012). Pairing measurements of the water vapor isotope ratio with humidity to deduce atmospheric moistening and dehydration in the tropical midtroposphere. Journal of Climate, 25(13), 4476–4494. https://doi.org/10.1175/JCLI-D-11-00582.1

Pagano, T. S., Aumann, H. H., Hagan, D. E., & Overoye, K. (2003). Prelaunch and in-flight radiometric calibration of the Atmospheric Infrared Sounder (AIRS). IEEE transactions on geoscience and remote sensing, 41(2), 265-273. 10.1109/TGRS.2002.808324

Pokam, W. M., Bain, C. L., Chadwick, R. S., Graham, R., Sonwa, D. J., & Kamga, F. M. (2014). Identification of processes driving low-level westerlies in West Equatorial Africa. Journal of Climate, 27(11), 4245–4262. https://doi.org/10.1175/JCLI-D-13-00490.1

Pokam, W. M., Djiotang, L. A. T., & Mkankam, F. K. (2012). Atmospheric water vapor transport and recycling in Equatorial Central Africa through NCEP/NCAR reanalysis data. Climate Dynamics, 38(9–10), 1715–1729. https://doi.org/10.1007/s00382-011-1242-7

Risi, C., Muller, C., & Blossey, P. (2020). What controls the water vapor isotopic composition near the surface of tropical oceans? Results from an analytical model constrained by large-eddy simulations. Journal of Advances in Modeling Earth Systems, 12(8). https://doi.org/10.1029/2020MS002106

https://doi.org/10.5194/egusphere-2025-4330
Preprint. Discussion started: 27 November 2025

Risi, C., Noone, D., Frankenberg, C., & Worden, J. (2013). Role of continental recycling in intraseasonal variations of continental moisture as deduced from model simulations and water vapor isotopic measurements. Water Resources Research, 49(7), 4136–4156. https://doi.org/10.1002/wrcr.20312

Rutan, D. A., S. Kato, D. R. Doelling, F. G. Rose, L. T. Nguyen, T. E. Caldwell, and N. G. Loeb. (2015): CERES synoptic product: Methodology and validation of surface radiant flux. J. Atmos. Oceanic Technol., 32, 1121–1143, doi: 10.1175/JTECH-D-14-00165.1.

Schiro, K. A., Ahmed, F., Giangrande, S. E., & David Neelin, J. (2018). GoAmazon2014/5 campaign points to deep-inflow approach to deep convection across scales. Proceedings of the National Academy of Sciences of the USA, 115(18), 4577–4582. https://doi.org/10.1073/pnas.1719842115

Sohn, B. J., Choi, M. J., & Ryu, J. (2015). Explaining darker deep convective clouds over the western Pacific than over tropical continental convective regions. Atmospheric Measurement Techniques, 8(11), 4573-4585. https://doi.org/10.5194/amt-8-4573-2015

Sorí, R., Stojanovic, M., Nieto, R., Liberato, M.L. & Gimeno, L. (2022). Spatiotemporal variability of droughts in the Congo River Basin: The role of atmospheric moisture transport. In Congo Basin Hydrology, Climate, and Biogeochemistry (eds R.M. Tshimanga, G.D.M. N'kaya and D. Alsdorf). 10.1002/9781119657002.ch11.

Su, W., T. P. Charlock, and F. G. Rose. (2005): Deriving surface ultraviolet radiation from CERES surface and atmospheric radiation budget: Methodology. J. Geophys. Res., 110(D14209), doi: 10.1029/2005JD005794.

Thorncroft, C. D., Nguyen, H., Zhang, C., & Peyrillé, P. (2011). Annual cycle of the West African monsoon: regional circulations and associated water vapour transport. Quarterly Journal of the Royal Meteorological Society, 137(654), 129-147. https://doi.org/10.1002/qj.728

Tremoy, G., Vimeux, F., Soumana, S., Souley, I., Risi, C., Favreau, G., & Oï, M. (2014). Clustering mesoscale convective systems with laser-based water vapor $\delta^{18}O$ monitoring in Niamey (Niger). Journal of Geophysical Research, 119(9), 5079–5103. https://doi.org/10.1002/2013JD020968

van der Ent, R. J., Savenije, H. H. G., Schaefli, B., & Steele-Dunne, S. C. (2010). Origin and fate of atmospheric moisture over continents. Water Resources Research, 46(9). https://doi.org/10.1029/2010WR009127

Washington, R., James, R., Pearce, H., Pokam, W. M., & Moufouma-Okia, W. (2013). Congo basin rainfall climatology: Can we believe the climate models? Philosophical Transactions of the Royal Society B: Biological Sciences, 368(1625). https://doi.org/10.1098/rstb.2012.0296

Worden, J., Kulawik, S., Frankenberg, C., Payne, V., Bowman, K., Cady-Peirara, K., et al. (2012). Profiles of CH_4, HDO, H_2O, and N_2O with improved lower tropospheric vertical resolution from Aura TES radiances. Atmospheric Measurement Techniques, 5(2), 397–411. https://doi.org/10.5194/amt-5-397-2012

Worden, J., Noone, D., Bowman, K., Beer, R., Eldering, A., Fisher, B., et al. (2007). Importance of rain evaporation and continental convection in the tropical water cycle. Nature, 445(7127), 528–532. https://doi.org/10.1038/nature05508

Worden, J., Saatchi, S., Keller, M., Bloom, A., Liu, J., Parazoo, N., et al. (2021). Satellite observations of the tropical terrestrial carbon balance and interactions with the water cycle during the 21st century. Reviews of Geophysics, 59, e2020RG000711. https://doi.org/10.1029/2020RG000711.

https://doi.org/10.5194/egusphere-2025-4330
Preprint. Discussion started: 27 November 2025

Worden, S., Fu, R., Chakraborty, S., Liu, J., & Worden, J. (2021). Where Does Moisture Come From Over the Congo Basin?. Journal of Geophysical Research: Biogeosciences, 126(8), e2020JG006024. https://doi.org/10.1029/2020JG006024

Wright, J. S., Fu, R., Worden, J. R., Chakraborty, S., Clinton, N. E., Risi, C., et al. (2017). Rainforest-initiated wet season onset over the southern Amazon. Proceedings of the National Academy of Sciences of the USA, 114(32), 8481–8486. https://doi.org/10.1073/pnas.1621516114

Xu, L., Saatchi, S., Yang, Y., Yu, Y., Pongratz, J., Bloom, A., et al. 2021. Changes in global terrestrial live biomass over the 21st century. Science Advances, 7(27): eabe9829. 18 p. https://doi.org/10.1126/sciadv.abe9829.

Yang, W., Seager, R., Cane, M. A., & Lyon, B. (2015). The annual cycle of East African precipitation. Journal of Climate, 28, 2385–2404. https://doi.org/10.1175/JCLI- D- 14- 00484.1

Zhang, Z., Xu, C. Y., El-Tahir, M. E. H., Cao, J., & Singh, V. P. (2012). Spatial and temporal variation of precipitation in Sudan and their possible causes during 1948–2005. Stochastic environmental research and risk assessment, 26, 429-441. https://doi.org/10.1007/s00477-011-0512-6

Zhou, L., Tian, Y., Myneni, R. B., Ciais, P., Saatchi, S., Liu, Y. Y., et al. (2014). Widespread decline of Congo rainforest greenness in the past decade. Nature, 508(7498), 86–90. https://doi.org/10.1038/nature13265